CHEMISTRY OF MATERIALS

pubs.acs.org/cm

Article

A Glance at Novel Ionanofluids Incorporating Silk-Derived Carbon Dots

Published as part of Chemistry of Materials virtual special issue "In Honor of Prof. Clement Sanchez".

Tiago A. G. Duarte,* Rui F. P. Pereira, Bruno Medronho, Elizaveta S. Maltseva, Elena F. Krivoshapkina, Alejandro Varela-Dopico, Pablo Taboada, Lianshe Fu, Rute A. S. Ferreira, and Verónica de Zea Bermudez*

Cite This: *Chem. Mater.* 2024, 36, 1136−1152

Read Online

ACCESS | Metrics & More | Article Recommendations | Supporting Information

ABSTRACT: One of the hallmarks of the current efforts in the field of thermal energy is heat transfer enhancement. Ionanofluids (INFs), a combination of nanomaterials and ionic liquids (ILs), are an appealing category of thermal fluids. In this work, we introduce sustainable INFs composed of carbon dots derived from *Bombyx mori* silk fibroin (SF) dispersed in a mixture of 1-butyl-3-methylimidazolium chloride (IL_1) and 1-(4-sulfobutyl)-3-methyl-imidazolium triflate (IL_2). The syntheses were performed at mild conditions, with reaction times of 3, 4, and 5 h, and without purification steps. The INFs display room-temperature emission in the visible spectral range with quantum yield values up to 0.09 and are essentially viscous fluids ($G'' > G'$). A marked shear thinning behavior is observed at high shear rates, particularly for the systems $SFIL_1IL_2$-3h and $SFIL_1IL_2$-4h. The INFs demonstrate relatively high heat capacity and thermal conductivity values in comparison to state-of-the-art INFs. Under suitable illumination conditions, the INFs can convert light into heat in an efficient manner, with photothermal conversion efficiencies of up to 28%, similar to other reported INFs. $SFIL_1IL_2$-5h exhibits remarkable stability over time within the range of working temperatures. This work paves the way for the development of new thermal fluids for enhanced heat transfer technologies using sustainable synthesis routes and natural raw precursor materials.

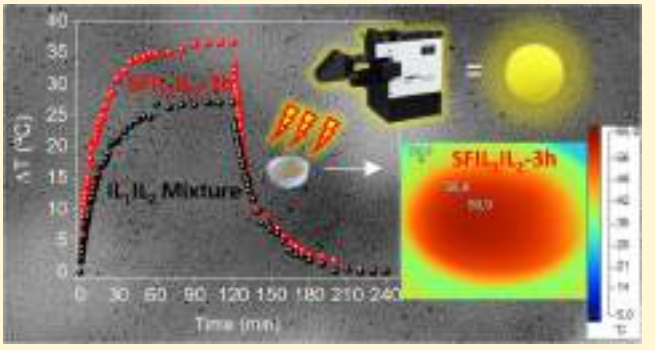

KEYWORDS: *ionanofluids, silk fibroin, carbon dots, imidazolium ionic liquids, thermal fluids*

INTRODUCTION

In recent decades, society has been facing serious global problems associated with world population growth, accelerated industrialization, expanding economies, and concomitant rising energy demand. The consequences have been dramatic, the gradual exhaustion of fossil fuel sources, the instability in oil and natural gas markets, the increasing release of greenhouse gas (GHG) emissions, the depletion of the ozone layer, and the melting of polar ice caps being major concerns. To add to this critical scenario, over the last few decades, the world has seen growing signs of climate change most probably linked to human activities. The steady rise of average global temperatures, together with the increasing frequency and severity of extreme weather events, pose serious hazards to energy infrastructures. If temperature thresholds are exceeded, energy supply to populations may be threatened in the future.[1] The increasing water scarcity, especially in dry climate regions, also affects dramatically all those activities of the energy sector relying on water cooling systems, such as mining, fuel production, hydropower generation, and nuclear power plants. As we write, the world finds itself in a global energy crisis as a consequence of the aftermath of the Covid-19 pandemic and the huge uncertainties associated with the ongoing armed conflicts in Europe and Africa.

Solar energy, a clean, abundant, endless, and freely accessible energy source, offers tremendous opportunities for achieving the transition to a clean and environmentally friendly renewable energy economy. Advances in solar energy technology have enabled its transformation from a niche business into a mature industry. However, although solar thermal and solar photovoltaic (PV) technologies have witnessed remarkable progress over the last decades, in terms of overall thermal performance they have both reached a limit,

Received: June 5, 2023
Revised: December 14, 2023
Accepted: December 15, 2023
Published: January 2, 2024

largely due to technical setbacks related to heat transfer phenomena.[2] It is known that from 25 to 80 °C,[3] the solar PV panel's efficiency starts decreasing by ca. 0.4−0.5% for each degree rise in temperature.[4,5] This effect is caused by the use of conventional working fluids (e.g., water and oils) which do not provide suitable thermophysical behavior. Yet, this technical drawback is not exclusive to the domain of solar energy. The need to fulfill the current cutting-edge technological requirements in terms of heat transfer has become a challenging topic in most engineering domains. Nowadays, more than ever, heat dissipation, heat harvesting, heat storage, heat transportation, and cooling represent paramount problems. Solving them will hopefully help find a way to tackle the energy crisis while meeting industrial, domestic, transportation, and electronics energy demands while mitigating environmental impacts and lowering costs.

In this context, one of the most promising solutions has emerged from the advent of nanofluids. Nanofluids, a breakthrough concept pioneered by Lee et al.,[6] are colloidal mixtures of nanometer-sized solid particles dispersed in a base fluid. In general, the base fluid is a low-viscosity liquid, like water, or a high-viscosity liquid, such as ethylene glycol (EG), mineral oil, or a mixture of liquids (e.g., EG−water or propylene glycol−water). Unlike conventional mixtures, nanofluids exhibit enhanced thermophysical properties, such as an abnormal heat capacity boost at low nanoparticle concentration[7] and a thermal conductivity conspicuously higher than that of the base fluid. Heat capacity and thermal conductivity but also viscosity and density are vital properties that dictate the usefulness of a nanofluid as a heat transfer fluid. The tremendous technological potential of nanofluids in a very wide array of thermal applications ranging from heat transfer devices to solar energy applications was immediately recognized.[8,9] In recent years, significant advances have been made in the use of nanofluids in solar collectors,[10−12] heat exchangers,[13,14] refrigeration systems,[15] radiators,[16] thermal storage systems,[17] solar thermal conversion,[18] and electronic cooling.[19]

The quest for the development of low-cost systems from renewable raw materials, and the use of sustainable and green syntheses, led to a resourceful and extremely attractive new category of nanofluids classed as ionanofluids (INFs).[20] INFs, considered by many as the next generation of heat transfer fluids, are composed of nanomaterials (usually metals and their oxides and carbon nanostructured materials, mostly tubes, fullerenes, and spheres) dispersed in a base fluid that can only include ionic liquids (ILs) or a mixture of an IL and water. The use of carbon dots (CDs) has been considerably less explored.[21−23] ILs have unique attributes, which include an eco-friendly character, a safe nature, recyclability, nonflammability at ambient temperature, negligible vapor pressure, excellent thermophysical properties (e.g., high thermal stability, high volumetric heat capacity, and wide viscosity range) compatible with the requisites of heat transfer fluids, and great versatility in terms of chemical composition (cation−anion structure with endless possibilities of combination), enabling the fine-tuning of their structure and tailoring of the properties to satisfy task-specific applications. Fukushima *et al.*[24] were the first to mix carbon nanotubes (CNTs) with ILs to produce a gel at room temperature which was termed "bucky gel". Awareness of the tremendous potential of INFs urged the study of these alternative fluids,[25] and to date, this class of thermal fluids has not ceased to attract the attention of the scientific community.[26,27]

Recently, some of us introduced a straightforward, clean, fast, cheap, single-step, and versatile method for producing self-standing, water-soluble, viscous, reusable CD-based INFs with self-improving conductivity, thermotropy around 30−40 °C, and ultraviolet (UV) radiation-blocking ability.[22] Glucose was the raw material selected for the synthesis of the CDs, whereas the base fluid chosen was the benign and commercially available 1-butyl-3-methylimidazolium chloride ([Bmim][Cl]) IL, playing the dual role of reaction media and functionalization molecule. The glucose/[Bmim][Cl] INF was employed in a thermotropic device (TTD) with surface plasmon resonance effect (SPRE)-boosted performance and in an integrated thermo-electro-optical device, both enabling modulation of solar light and heat.[22] The integrated device operated either in thermotropic or electrochromic modes, offering impressive memory effect, excellent cycling stability, and colossal coloration efficiency. A similar approach was subsequently employed for the development of an analogous INF derived from biomass waste (chitin from crab shells).[23] In the latter case, the homemade 1-tosylate-3-methylimidazolium triflate IL was added to facilitate the cleavage of the glycoside bonds present in chitin. All these features render this class of high-performance thermosensitive INFs potentially attractive not only for smart window technology but also for the energy coatings sector and for heat transfer systems, among other fields.

Herein, inspired by the two aforementioned works,[22,23] we extend our sustainable INF strategy by employing a natural protein as raw material for the production of the CDs. Our choice fell on silk fibroin (SF), the core protein of silk fibers originating from *Bombyx mori* (*B. mori*) cocoons, because of the great potential of silk-derived materials for energy devices. Some of us reported the first SF[28]- and cocoon[29,30]-based separators for lithium batteries, proposed novel highly conductive SF-based electrolytes,[31] and developed a new solvent platform for SF.[32] To the best of our knowledge, the use of protein-based biomass derivatives as a carbon source for the synthesis of CDs under mild conditions in an IL medium is unprecedented. Usually the CD syntheses from proteins require a hydrothermal treatment at high temperature and pressure,[33] a strong acid medium,[34] or microwave (MW) irradiation.[35] All of these methods include subsequent purification steps, which are simply avoided in the present processing of the SF-derived INFs, an aspect that represents a major advantage if scaling up is envisaged. At last, it is worth mentioning that the preparation of CDs from SF under the mild conditions proposed here contrasts markedly with those reported in the literature, since solely the hydrothermal treatment[36] and MW irradiation[37] were previously attempted.

Thus, in the present work, we develop a new family of INFs composed of CDs derived from *B. mori*-based SF and a mixture of ILs comprising [Bmim][Cl] and 1-(4-sulfobutyl)-3-methylimidazolium triflate ([SBmim][Trif]). The latter IL, employed as the acid catalyst for different organic reactions,[38,39] was added to induce the acid hydrolysis and degradation of the protein into smaller peptides and then into the amino acids, which are the building blocks for the CDs' formation. The structure, size, shape, and surface functional groups of the CDs are investigated. The rheological properties of the INFs are studied and the optical features of the INFs and of the corresponding dilute aqueous solutions are examined. At last,

https://doi.org/10.1021/acs.chemmater.3c01370
Chem. Mater. 2024, 36, 1136−1152

Scheme 1. Representation of the Synthesis of the INFs

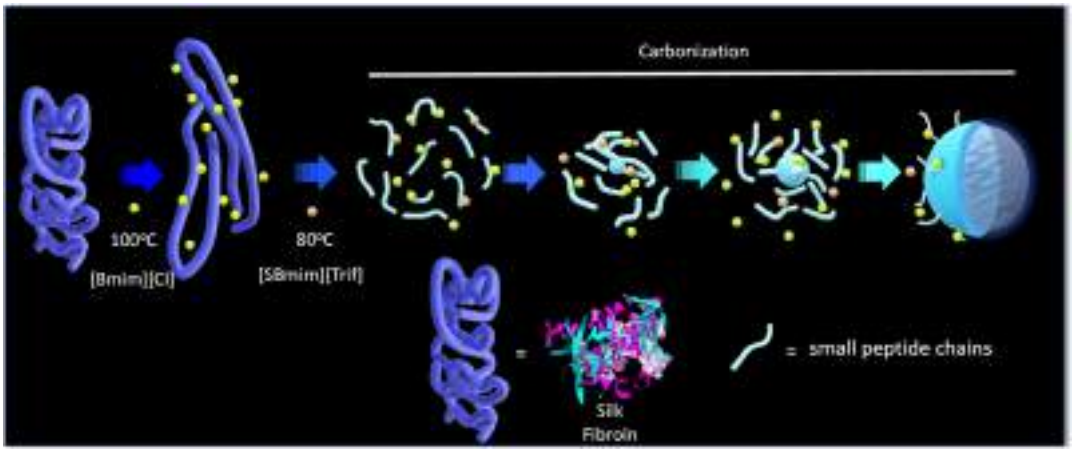

the potential of the INFs for thermal energy applications is evaluated.

EXPERIMENTAL SECTION

Materials and Chemicals. *B. mori* cocoons were supplied by APPACDM from Castelo Branco (Portugal). 1-Butyl-3-methylimidazolium chloride ([Bmim][Cl], IL_1, Acros Organics, 98%), 1-(4-sulfobutyl)-3-methylimidazolium triflate ([SBmim][Trif], IL_2, BLDpharm, 98.46%), anhydrous sodium carbonate (Na_2CO_3, Sigma-Aldrich, 99.9%), anhydrous lithium bromide (LiBr, Thermo Scientific, 99%), *n*-decane (Sigma-Aldrich ≥99%), and squalene (Sigma-Aldrich ≥99%) were used as received unless stated otherwise. Slide-A-Lyzer G2 dialysis cassettes (molecular-weight cutoff of 3.5 kDa) were purchased from Thermo Fisher Scientific. High-purity Milli-Q water (resistivity 18 MΩ cm, Interlab System Purist UV set) was used in all aqueous solutions.

Preparation of Solid SF. To obtain SF from *B. mori* silk cocoons, the degumming method reported by Rockwood *et al.*[40] was adopted. Briefly, a mass of 5 g of *B. mori* silkworm cocoons was cut into small pieces and cleaned. The chopped pieces were transferred into a boiling 0.02 M Na_2CO_3 aqueous solution with a volume of 2 L where they remained for 30 min. The fibers were removed from this solution and rinsed in water to remove excess Na_2CO_3. After repeating the last step thrice, the fibers were squeezed and dried in an oven at 60 °C. To prepare the SF solution, a 9.3 M LiBr aqueous solution with a volume of 20.5 mL was added to the SF fibers and maintained for 4 h at 60 °C until all the fibers were dissolved. The LiBr−silk solution was transferred to a dialysis cassette (3500 kDa) and dialyzed against ultrapure water. The dialyzed silk solution was centrifuged twice at 4000 rpm for 20 min to remove any solid impurities. The concentration of the final SF solution was determined by measuring the dry weight (6.8 w/v %). To prepare SF powder for further studies, the solution was lyophilized. Frozen samples were placed in a lyophilizer for 7 days until complete drying. The resulting SF was stored at 4 °C.

INF Synthesis. The synthesis was inspired by previous works reported in the literature.[21,41] Briefly, 2 g of IL_1 was placed in a 50 mL round-bottom flask and was maintained for 30 min at 80 °C with constant magnetic stirring. Then, 0.2 g of mechanically crushed SF powder was added to IL_1 and maintained for 1 h at 100 °C until complete SF dissolution. Afterward, 0.2 g of pure IL_2 was added to the mixture and left to react for 3 h at 80 °C. Two other syntheses were performed in which the only change introduced was extending the reaction time to 4 and 5 h (Scheme 1). The samples were designated $SFIL_1IL_2$-3h, $SFIL_1IL_2$-4h, and $SFIL_1IL_2$-5h, respectively. After cooling, the resulting products demonstrated viscous consistency, yellowish hue under visible light, and blue, violet, and pink color under UV irradiation of 365 nm, respectively (Scheme S1).

Characterization. High-resolution transmission electron microscopy (TEM) images were recorded at the Iberian Nanotechnology Laboratory (INL)-Portugal using a double-corrected FEI Titan G3 Cubed Themis working at an acceleration voltage of 200 kV. The samples (previously diluted 1/20 in water) were prepared by drop-casting the solution onto a 400 mesh Cu grid containing a continuous carbon support film (Ted Pella ref 01824). The samples were incubated for 3 min on the grid, and then the solution was blotted off.

Attenuated total reflectance/Fourier transform infrared (ATR/FTIR) spectra of the INFs and the IL_1IL_2 mixture were recorded in a Shimadzu IRAffinity 1 s Fourier transform infrared spectrophotometer equipped with a diamond crystal. Before measurement, a small amount of each sample was transferred to the diamond crystal and pressed. The spectra were recorded at room temperature in the 4000−400 cm^{-1} range by averaging 64 scans with a resolution of 4 cm^{-1}. Data was processed using LabSolutions IR software.

X-ray photoelectron spectroscopy (XPS) spectra were obtained on an ESCALAB 250Xi (ThermoFisherScientific) with a hemispherical analyzer at INL. The X-ray source was monochromated Al Kα ($h\nu$ = 1486.68 eV) radiation, operated at 220 W and 14.6 kV, and the spot size set at 650 mm. The XPS spectra were collected at pass energies of 100 and 40 eV for survey spectra and individual elements, respectively. The energy step for individual elements was 0.1 eV. The XPS band envelope analysis was performed using the iterative least-squares curve-fitting procedure in PeakFit software.[42] The best fit of the experimental data was obtained by varying the frequency, bandwidth, and intensity of the bands. Band fitting was conducted using a Voigt function, using a linear baseline correction with a tolerance of 0.2%. The standard errors of the curve-fitting procedure were less than 0.002. The samples were drop-cast on gold-coated Si wafers and mounted on a 20 × 50 mm sample holder (Thermo Fisher Scientific).

The TGA curves were recorded in a NETZSCH STA 449F3 thermal analyzer equipped with Proteus software under a nitrogen atmosphere (20 cm^3 min^{-1} flow rate), with a heating rate of 10 °C min^{-1}. Before measurement, the sample, with a mass of 5 mg, was transferred to an open alumina (Al_2O_3) crucible.

The rheological assays were monitored under steady and oscillatory modes in a HAAKE MARS III rheometer (Thermo Fisher Scientific, Karlsruhe, Germany) set with a plate−plate geometry (35 mm, 1 mm gap). A Peltier unit was used to ensure strict temperature control, while a solvent trap was employed to prevent moisture absorption. The storage modulus (G'), the loss modulus (G''), and the complex viscosity (η^*) were assessed by dynamic oscillatory assays performed in a frequency range of 0.01−50 Hz within the linear viscoelastic regime (the selected stress was 2 Pa). Nonlinear rotational assays were performed by varying the applied shear rate ($\dot{\gamma}$) from 0.1 to 150 s^{-1}. The viscoelastic parameters G', G'', and η^* were also evaluated with temperature sweep assays from 25 to 80 °C and back to 25 °C. The heating rate was set to 2 °C min^{-1}, while the cooling rate was 4-

https://doi.org/10.1021/acs.chemmater.3c01370
Chem. Mater. 2024, 36, 1136−1152

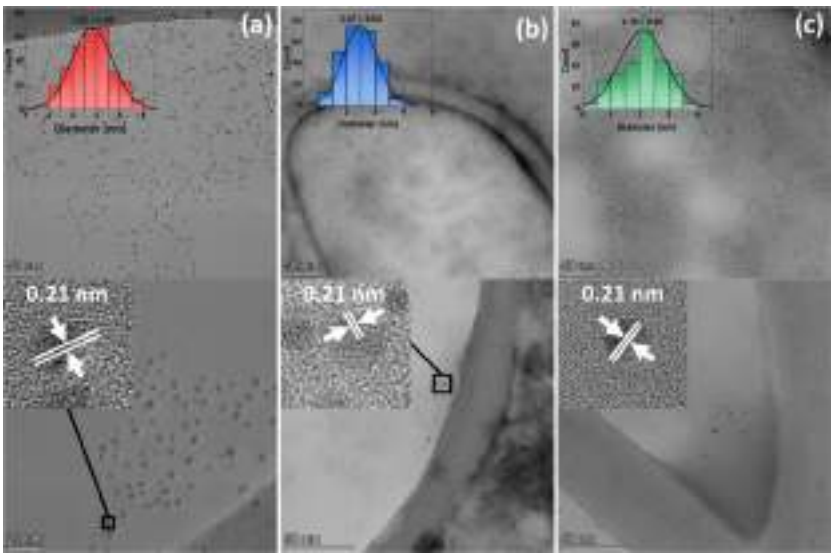

Figure 1. TEM images of the CDs in the INFs: (a) $SFIL_1IL_2$-3h, (b) $SFIL_1IL_2$-4h, and (c) $SFIL_1IL_2$-5h. Inset images show the histogram size distribution of the CDs and high-resolution TEM images of individual CDs showing lattice fringes with the corresponding *d*-spacing determined by FFT analysis.

fold lower (0.5 °C min^{-1}) to ensure thermal equilibrium. A constant stress (2 Pa) and frequency (1 Hz) were applied in both heating and cooling ramps.

UV−visible absorption spectra were recorded with a UV−vis spectrophotometer (U-4100) using a 10 mm path quartz cuvette. The aqueous solutions were prepared by dissolving 20 mg of the sample in 6 mL of distilled water (0.33% weight).

Transmittance spectra were recorded in the 400−1650 nm range using a DH Mini UV−vis−NIR Light Source from Ocean Optics. Aqueous solutions were prepared by dissolving different contents of IL_1IL_2 mixture or $SFIL_1IL_2$-3h (0.33, 0.66, 1.00, 1.33, and 1.66% w) in 6 mL of water.

The photoluminescence spectra were recorded at room temperature with a modular double-grating excitation spectrofluorimeter with a TRIAX 320 emission monochromator (Fluorolog-3, Horiba Scientific) coupled to an R928 Hamamatsu photomultiplier. The excitation source was a 450 W Xe arc lamp. The emission spectra were corrected for detection and the optical spectral response of the spectrofluorimeter, and the excitation spectra were corrected for the spectral distribution of the lamp intensity using a photodiode reference detector. The absolute emission quantum yield (Φ) values were measured at room temperature using a C9920-02 Hamamatsu system. The method is accurate within 10%.

Specific heat capacities were obtained via the isothermal step method with a Micro DSCIII differential scanning calorimeter from Setaram, France. Calibration was performed using a Joule effect calibration vessel (Setaram) and checked using *n*-decane and squalene as heat capacity standards, their C_p values being taken from the literature.[43,44] Background noise of the Micro DSCIII was less than 3 μW. The standard uncertainty in C_p experimental values is estimated to be 0.002 J g^{-1} K^{-1}, as previously reported by Marques *et al.*[45]

Thermal conductivity measurements were performed in a liquid nitrogen cryostat using the 3ω method in a homemade setup.[46] The heater/sensor was a Pt resistance (1 mm long, 10 μm wide, and 100 nm thick) deposited by optical lithography on a low-thermal conductivity glass. For the measurements, a small amount of the sample (≈100 μg) was deposited on top of the platinum resistance, and thermal conductivity was measured during thermal scan rates of 1 K min^{-1} from the 3ω voltage at 76 and 362 Hz [linearity of 3ω vs ln(2ω) was verified between 10 Hz and ≈500 Hz]. Unfortunately, the only statistically significant data of this parameter were obtained at room temperature (25 °C) since, at higher ones, the ILs degraded the Pt line leading to signal fluctuations that did not allow us to achieve suitable reproducibility.

Irradiation experiments were done using a setup consisting of a Teflon petri dish with a diameter of 5.1 cm where ca. 3 g of the sample (except for water used as a control, 6 g) was deposited. For irradiation experiments, the dish was set at a distance of 8 cm from the solar simulator (ABET SunLite model 11002, Abet Technologies, USA) equipped with a 100 W Xe arc lamp and 1.5G filter, which was calibrated to achieve an intensity of 1 Sun. After turning on the light source for 2 h and turning it off for another 2 h, temperature changes upon irradiation were measured using a Fluke TIS75-30 Hz Fluke Thermal Imager with Fluke Connect & IR-Fusion technology with 320 × 240 resolution. For the reusability test, the sample was irradiated for 1 h with the light source on and then remained for 90 min with the light source off.

The bulk temperature distribution of the INFs was accessed by irradiating 2 mL of each sample in quartz cuvettes with a Oriel Illumination system (model APEX2-XE, Oriel Instruments, USA) equipped with a xenon lamp of 100 W. Samples were located at a distance of ca. 3 cm and irradiated at ca. 1 cm from the upper liquid surface. The bulk temperature distribution was evaluated at different time intervals (from 30 s up to 5 min) using a thermal imaging camera (FLIR E75, FLIR Systems, USA).

The photothermal conversion efficiency (η_{pc}) of the INFs was evaluated using two different models. In the first one, η_{pc} was calculated by considering only the useful energy absorbed by the INFs regarding the incident radiation without considering the heat dissipation to the environment by using the following equation

$$\eta_{pc} = \frac{m_{nf} c_{nf} \Delta T}{I_0 A \Delta t} \quad (1)$$

where m_{nf}, c_{nf}, ΔT, I_0, A, and Δt are the mass and specific heat of the INF, the difference between the initial and the instantaneous temperatures, the heat flux of the incident solar (W m^{-2}), the irradiated area (m^2), and the time exposed to light radiation (s), respectively. The above model does not consider thermal losses from the INFs and, thus, η_{pc} decreases with increasing operating temperature due to incremental thermal losses. In the second model, the energy conservation equation, including the loss term, is written as[47]

$$m_{nf} c_{nf} \frac{dT}{dt} + Q_{loss} = I_o A \eta \quad (2)$$

where Q_{loss} is the thermal loss to the surroundings, which is a function of temperature, and can be expressed as

https://doi.org/10.1021/acs.chemmater.3c01370
Chem. Mater. 2024, 36, 1136−1152

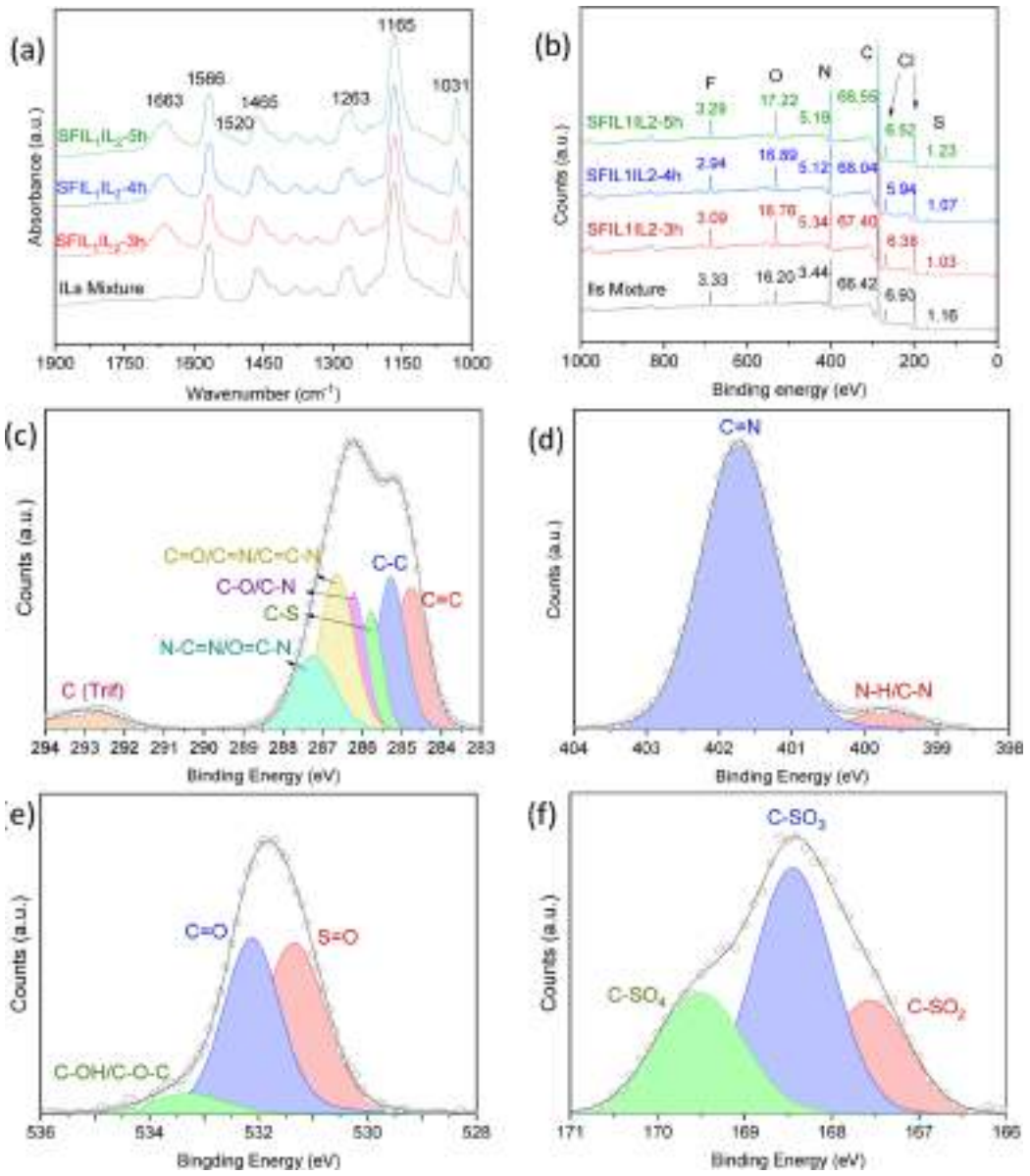

Figure 2. (a) ATR/FTIR and (b) XPS survey spectra of the $SFIL_1IL_2$-3h (red line), $SFIL_1IL_2$-4h (blue line), and $SFIL_1IL_2$-5h (green line) INFs and of the IL_1IL_2 mixture (black line). In (b), the elemental composition (in %) is indicated over the respective peak. XPS spectra of the (c) C 1s, (d) N 1s, (e) O 1s, and (f) S 2p peaks of $SFIL_1IL_2$-3h, where blank dots are XPS raw data and the black line is the fitting curve (see Experimental Section for details).

$$Q_{loss} = hA_{loss}[(T(t) - T_{amb})] \quad (3)$$

where h is the heat transfer coefficient, A_{loss} is the surface area of heat dissipation, $T(t)$ is the temperature of the nanofluids at time t, and T_{amb} is the ambient temperature. Thus, revising eq 2, this can be expressed as

$$\frac{dT}{dt} = \frac{AI_0\eta}{m_{nf}c_{nf}} - B[(T(t) - T_{amb})] \quad (4)$$

where B is the rate constant of heat dissipation. At the equilibrium stage, that is, when the photothermal heating equals the thermal dissipation, $\frac{dT}{dt} = 0$ and thus

$$\frac{AI_0\eta}{m_{nf}c_{nf}} = B[T_{eq} - T_{amb}] \quad (5)$$

where T_{eq} is the equilibrium temperature. B can be derived from the slope of the linear plot of $\ln\left(\frac{T(t) - T_{amb}}{T_{eq} - T_{amb}}\right)$ vs t when the heat input becomes zero as the solar simulator is shut down. Therefore, the photothermal efficiency η_{pc} can be derived as

$$\eta_{pc} = \frac{Bm_{nf}c_{nf}[(T_{eq} - T_{amb})]}{AI_0} \quad (6)$$

RESULTS AND DISCUSSION

Characterization of the CDs. The TEM images shown in Figure 1a–c demonstrate that regardless of the reaction time, CDs with a uniform and nearly spherical shape are observed in all three INFs. The average diameters deduced for the CDs obtained with reaction times of 3, 4, and 5 h are 3.82 ± 0.86, 2.47 ± 0.60, and 2.10 ± 0.80 nm, respectively (Figure 1a–c). The decrease in the CD size with the increase in reaction time may be due to the loss of functional groups or to the loss of crystallinity.[48] High-resolution TEM measurements revealed well-resolved lattice fringes with an interplanar spacing of 0.21

https://doi.org/10.1021/acs.chemmater.3c01370
Chem. Mater. 2024, 36, 1136−1152

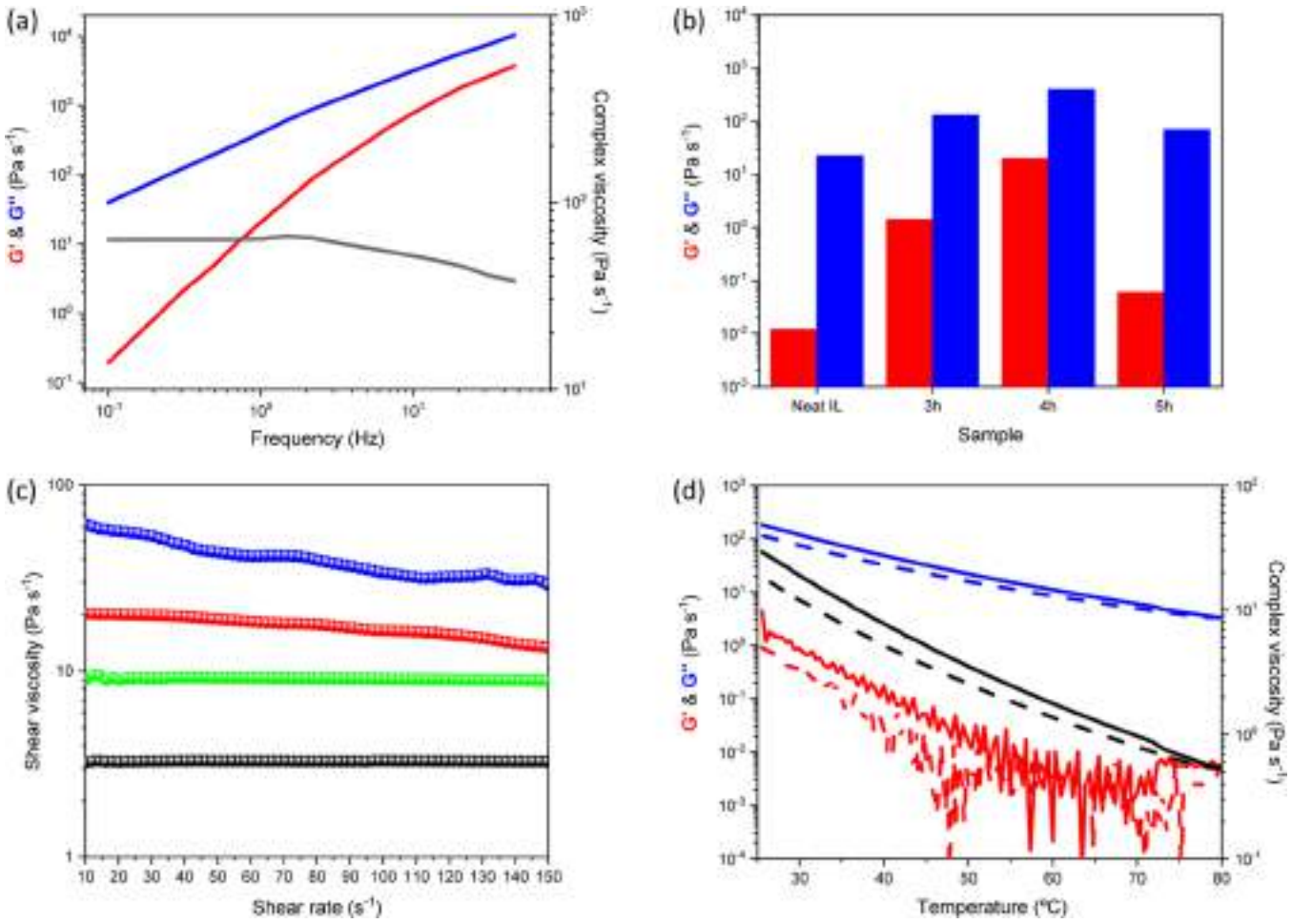

Figure 3. (a) Storage (red line), loss (blue line) moduli, and complex viscosity (black line) as a function of the oscillatory frequency for the sample prepared with $SFIL_1IL_2$-4h. (b) Viscoelastic parameters G' (red bars) and G'' (blue bars) at 1 Hz for the different reaction times. The neat IL_1IL_2 mixture is included for comparison. The dynamic frequency sweep tests were performed at 20 °C with the constant stress of 2 Pa. (c) Flow curves at 20 °C of the INFs $SFIL_1IL_2$-3h (red symbols); $SFIL_1IL_2$-4h (blue symbols); and $SFIL_1IL_2$-5h (green symbols). The neat mixture of ILs (black symbols) is also shown for comparison. (d) Viscoelastic parameters G' (red symbols), G'' (blue symbols), and complex viscosity (black symbols) as a function of the temperature cycle from 25 to 80 °C and back to 25 °C. The heating rate was defined as 2 °C min^{-1}, whereas the cooling rate was set to 0.5 °C min^{-1}. Constant stress (2 Pa) and frequency (1 Hz) were applied in both ramps.

nm (insets of Figure 1), which corresponds to the (100) diffraction planes of graphene.[41]

The mid-infrared ATR/FTIR spectra of the INFs and of the IL_1IL_2 mixture are represented in Figure S1. In the 1900−1000 cm^{-1} region (Figure 2a), the bands detected at 1566 and 1465 cm^{-1} correspond to the characteristic vibrations of the skeleton structure of the imidazolium ring,[49] whereas that at 1165 cm^{-1} is assigned to the bending vibration of the CH groups and asymmetric CF stretching vibration.[50] The bands at 1263 and 1031 cm^{-1} are associated with the asymmetric and symmetric stretching vibrations of SO_3 groups, respectively.[51] Regarding the INF signature, the band at 1663 cm^{-1} is the most evident fingerprint of the SF chains, being attributed to the vibration mode of the amide I group.[31,52] In addition to the amide I band (1750−1585 cm^{-1}), the amide II (1585−1485 cm^{-1}) and amide III (1285−1195 cm^{-1}) bands are usually also used to characterize the conformations of the SF protein.[31,52] In the present case, the latter two bands are overlapped with vibration modes associated with the mixture of ILs, and only one shoulder at 1520 cm^{-1} (absent in the spectrum of the IL_1IL_2 mixture) can be assigned to the presence of the amide II mode. The above spectral evidence led us to the conclusion that the degradation of the SF chains was not complete.

The XPS survey spectra of the INFs and the neat IL_1IL_2 mixture represented in Figure 2b allow us to distinguish seven peaks at 688.59, 531.76, 401.74, 286.56, 283.24, 197.13, and 168.16 eV, corresponding to F 1s, O 1s, N 1s, C 1s, Cl 1s, Cl 2p, and S 2p, respectively. The elemental composition of each sample reveals the same S/Cl weight ratio (around 1/6). As expected, the amounts of C, N, and O increase in the INFs compared to those in the IL_1IL_2 mixture.

The XPS spectra of C 1s, O 1s, N 1s, and S 2p for the INF synthesized with a 3 h reaction are shown in Figure 2c−f. In the high-resolution C 1s spectrum (Figure 2c), the signals of seven distinct carbon states distinguished at 284.8, 285.3, 285.8, 286.2, 287.7, 287.3, and 292.9 eV are ascribed to C═C, C−C, C−S, C−O/C−N, C═O/C═N/C═C−N, N−C═N/O═C−N, and C(Trif) groups, respectively.[21,53,54] The high-resolution N 1s spectrum (Figure 2d) was deconvoluted into two peaks at 399.7 and 401.7 eV, which represent N 1s states in N−H/C−N and C═N groups, respectively.[55] The O 1s spectrum shown in Figure 3e displays three peaks at 531.3, 532.1, and 532.9 eV, which are attributed to S═O, C═O, and

https://doi.org/10.1021/acs.chemmater.3c01370
Chem. Mater. 2024, 36, 1136−1152

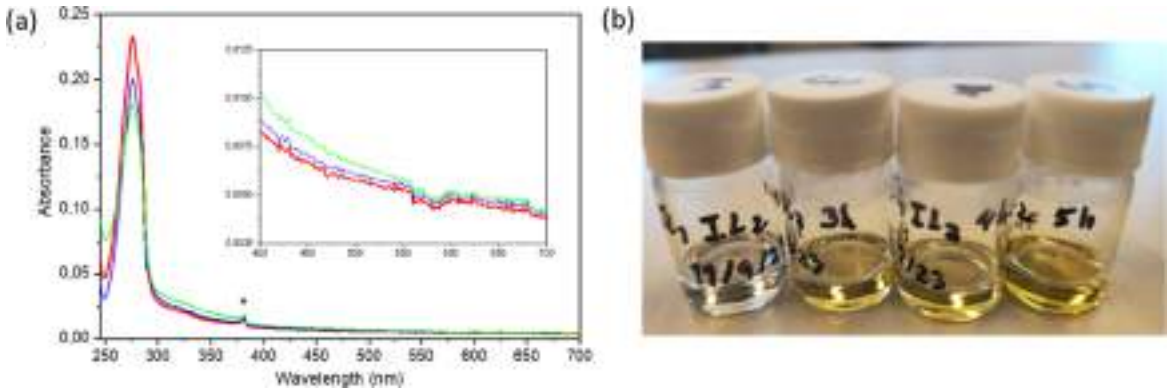

Figure 4. (a) Room-temperature UV−visible absorption spectra for the aqueous solutions of $SFIL_1IL_2$-3h (red line), $SFIL_1IL_2$-4h (blue line), and $SFIL_1IL_2$-5h (green line). The inset is an enlargement of the 400−700 nm spectral region. *Peak from the transition of the equipment lamp. (b) From left to right: physical appearance of IL_1IL_2, $SFIL_1IL_2$-3h, $SFIL_1IL_2$-4h, and $SFIL_1IL_2$-5h.

C−OH/C−O−C groups, respectively.[56] The high-resolution S 2p spectrum (Figure 2f) was deconvoluted into three peaks at 167.6, 168.4, and 169.5 eV, corresponding to the following different forms of sulfur: $-C-SO_x$, where x = 2, 3, and 4, respectively.[21,57]

The high-resolution XPS spectra of the other two INFs, reproduced in Figure S2, exhibit the same deconvoluted bands for the different elements. In contrast, the high-resolution C_{1s} spectrum of the neat IL_1IL_2 mixture, also reported in Figure S2, reveals the absence of the deconvoluted band of C═C at 284.8 eV but the presence of the expected C═C−N band at 287.1 eV.[54] Therefore, the emergence of a new band characteristic of the C═C bond in the high-resolution XPS spectra of the INFs corroborates the TEM findings and, thus, the existence of CDs. We emphasize that the SF XPS spectrum does not contain the C═C band either.[58−61] In addition, the high-resolution O 1s and N 1s spectra of the neat IL_1IL_2 mixture only display a single band, as typically found for ILs. In the case of the O 1s spectrum, this band, which was attributed to the S═O bond, appears at 532.1 eV, and in the N 1s spectrum, the band that emerges at 402.1 eV is associated with the C−N and C═N bonds.[54]

To get insight into the thermal stability of the INFs, TGA analyses were performed. The resulting TGA curves, reproduced in Figure S3, reveal that the thermal decomposition of $SFIL_1IL_2$-3h, $SFIL_1IL_2$-4h, $SFIL_1IL_2$-5h, and IL_1IL_2 mixture is a two-stage process. It is noteworthy that the four curves are practically coincident. The first stage, which occurs below 160 °C, involves the release of water (approximately 7, 9, 8, and 9%, respectively). The second stage encompasses a major thermal degradation with onset at 253, 254, 255, and 254 °C, respectively. This thermal event is characteristic of the decomposition of imidazolium-based ILs, as reported by Han et al.[62] The thermal degradation of SF residues, which is reported to occur between 250 and 400 °C,[63] might also contribute to this sharp and significant weight loss observed.

Rheological Survey of the INFs. The physical properties of the INFs play a key role, dictating their application. Rheometry is of great value with regard to the evaluation of the interplay between force, time, and deformation of matter. This is crucial in many areas, ranging from the in-depth materials characterization and support to complementary research methods up to product/process development and optimization. In this regard, nanotechnology considerably benefits from rheological insight. Nanodispersions, such as INFs, typically exhibit complex rheological features, which may be boosted by other effects, such as nanoparticle morphology, temperature, or solvent composition.[64−68]

Figure 3a displays a typical frequency (freq) sweep mechanical spectrum for the sample $SFIL_1IL_2$-4h. As can be seen, G'' is always higher than G', suggesting that this sample is essentially viscous over the entire frequency range studied. Similar behavior has been found in other systems.[69,70] The moduli follow a scaling; $G' \propto \text{freq}^2$, whereas $G'' \propto \text{freq}$, which is observed for polymer melts and viscous solutions.[71] The complex viscosity is found to reach a Newtonian plateau at low frequencies. For easier comparison, G' and G'' were replotted at a constant frequency (1 Hz) for the different reaction times considered (Figure 3b). The first striking observation is that all the INFs present higher G' and G'' than the neat mixture of ILs. The presence of CDs affects the flow of the ILs, and this has been described for related systems.[64] The viscoelastic parameters G' and G'' increase when the reaction time increases from $SFIL_1IL_2$-3h to $SFIL_1IL_2$-4h. Further increase in the reaction time ($SFIL_1IL_2$-5h) results in poorer G' and G'', meaning that the sample became more fluid-like.

Nonlinear rotational tests were performed and flow curves were obtained for all the samples (Figure 3c). In agreement with the dynamic oscillatory tests, the neat IL_1IL_2 mixture presents the lowest viscosity. It is essentially Newtonian, but a shear thinning behavior (barely perceptible in the log-scale) is observed at higher shear rates. Similar behavior is evident for the INFs synthesized for longer periods (i.e., 5 h). The synthesized $SFIL_1IL_2$-3h and $SFIL_1IL_2$-4h present the highest apparent viscosity and a marked shear thinning behavior over the shear rate window (from 10 to 150 s^{-1}). $SFIL_1IL_2$-4h presents the highest viscosity in agreement with the dynamic oscillatory tests (Figure 3a).

These novel INFs show a decrease in the viscoelastic parameters upon heating (Figure 3d). Such behavior is essentially reversible upon cooling, with a minor hysteresis observed. Since the cooling rate (0.5 °C min^{-1}) was four times lower than the heating rate (2 °C min^{-1}), it is reasonable to assume that energy dissipation and thermal equilibrium were achieved, and hence, the observed hysteresis has a different reasoning. Due to the inherent complexity of these systems, interparticle and IL ion interactions and reorganization are expected to be strongly dependent on temperature. Therefore, such effects should be also manifested in the observed hysteresis.[72] Moreover, these complex fluids are very sensitive

https://doi.org/10.1021/acs.chemmater.3c01370
Chem. Mater. 2024, 36, 1136−1152

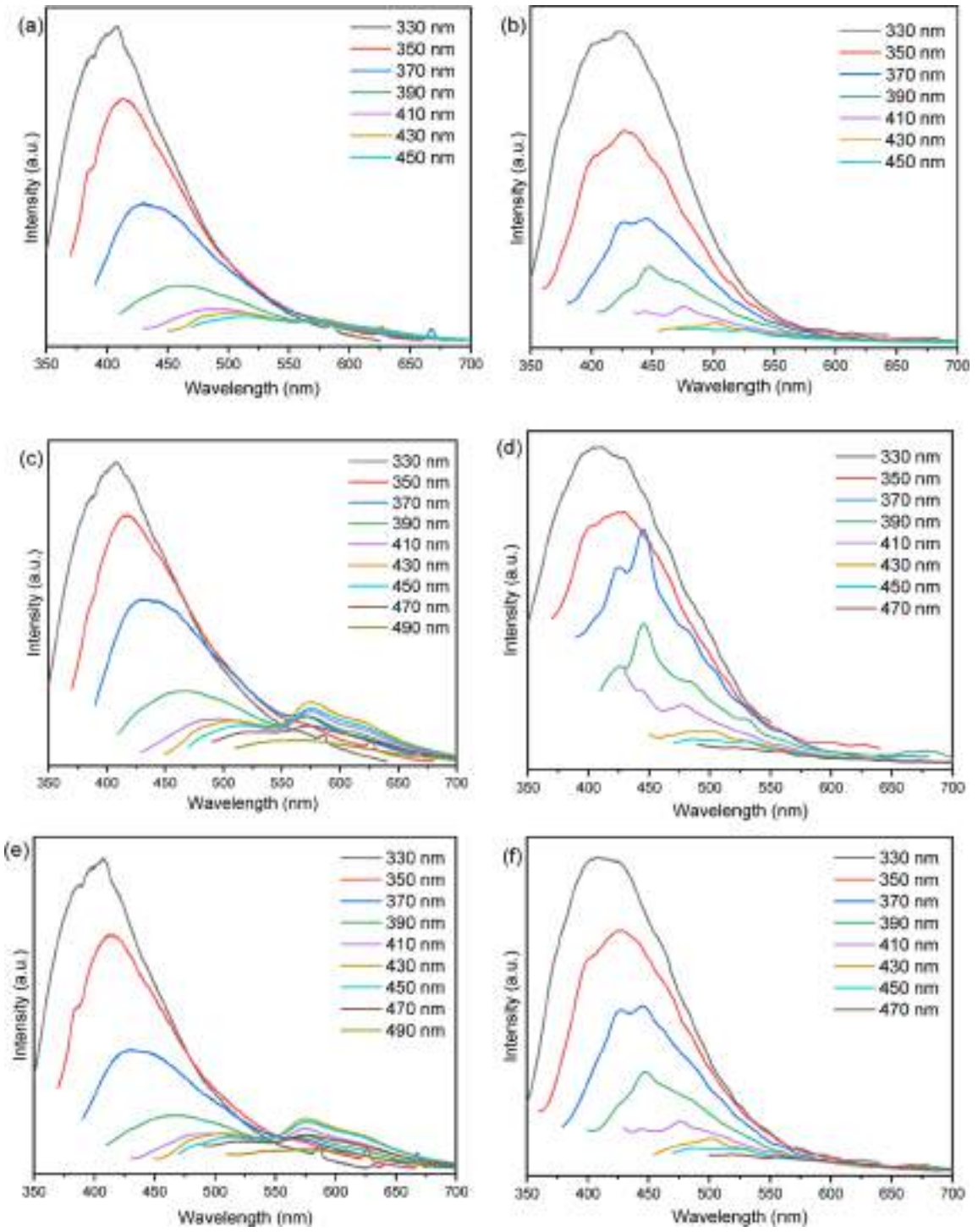

Figure 5. Emission spectra of the INFs (left column) and corresponding aqueous solutions (right column): (a,b) $SFIL_1IL_2$-3h, (c,d) $SFIL_1IL_2$-4h, and (e,f) $SFIL_1IL_2$-5h.

to shear history and moisture adsorption, and it is realistic to expect a small contribution of both these aspects in the detected hysteresis, despite the use of a solvent trap.

Optical Properties of the INFs. The optical properties of IL_1, IL_2, and the corresponding mixture and those of the INFs based on SF-derived CDs were characterized using UV−visible absorption and photoluminescence spectroscopy.

The UV−visible absorption spectrum of the IL_1IL_2 aqueous solution shows a weak broadband centered at around 310 nm (Figure S4), which can be ascribed to the $\pi-\pi^*$ transitions within the imidazolium units. On the other hand, the UV−visible absorption spectra of dilute aqueous solutions of $SFIL_1IL_2$-3h, $SFIL_1IL_2$-4h, and $SFIL_1IL_2$-5h display strong absorption peaks centered at 276 nm, which are ascribed to the $\pi-\pi^*$ transition of C═C groups in the sp^2 domain[73,74] (Figure 4). The UV−visible data are consistent with the band detected at 1566 cm^{-1} in the ATR/FTIR spectra attributed to the C═C vibrational modes of the imidazolium ring (Figures 2a and S1) and with the signal at 284.8 eV in the XPS spectra (Figures 2c and S2a). The weak absorption bands discerned in

https://doi.org/10.1021/acs.chemmater.3c01370
Chem. Mater. 2024, 36, 1136−1152

the 300−370 nm spectral region (Figure S4) are attributed to $n-\pi^*$ transitions of the C═O/C═N groups.[75] The latter finding is in agreement with the band at 1663 cm^{-1} in ATR/FTIR spectra (Figures 2a and S1), assigned to the SF amide groups, and with the 287.7 eV peak in the C 1s XPS spectra (Figures 2c and S2a). In the lower energy region (Figure S4), the appearance of the broad and weak absorption bands indicates that the three INFs possess different surface states.[76] This long-tailed absorption band becomes more evident with the increase in the reaction time as a result of the presence of more functional groups from IL_1 and IL_2 at the surface of the CDs (inset of Figure 4a).[77] The color change from light yellow to yellow for the INFs synthesized with reaction times of 3−5 h is a manifestation of this effect (Figure 4b).

The excitation and emission spectra of IL_1, IL_2, and IL_1IL_2, represented in Figure S5, reveal weak luminescence. The IL_1 solution shows excitation-independent emission at about 330 nm and excitation-dependent emission with the successive increasing excitation wavelength. In contrast, the IL_2 solution solely displays the excitation-dependent emission feature in the longer spectral region. Accordingly, the bands at around 340 nm in the mixture IL_1IL_2 can be attributed to the emission from IL_1 and the excitation-dependent emission bands can be ascribed to the emission of IL_1 and IL_2.

The INFs obtained at different reaction times are viscous solutions that exhibit, as noted above, a yellowish hue under visible light. Under UV irradiation of 365 nm, $SFIL_1IL_2$-3h shows blue color due to the dominant emission at around 400 nm (Figure 5a). For $SFIL_1IL_2$-4h (Figure 5c) and $SFIL_1IL_2$-5h (Figure 5e), the emission is a combination of the emission bands at 400 and around 575 nm (Scheme 1).

The emission spectra of the INFs in bulk and in aqueous solution at different excitation wavelengths are reproduced in Figure 5. In the case of $SFIL_1IL_2$-3h, when the excitation wavelengths are changed from 330 to 450 nm, all the emission spectra show broad bands with the maximum peaks shifting from 400 to 570 nm and the emission intensity decreasing (Figure 5a). The red-shift of the emission wavelength with increasing excitation wavelength indicates the excitation-dependent feature of these INFs. The different surface state energy levels from the various functional groups on the surface of INFs result in various emissive traps that dominate the different emission bands by changing the excitation wavelengths.[78] The same luminescence trend is observed for $SFIL_1IL_2$-4h (Figure 5c) and $SFIL_1IL_2$-5h (Figure 5e). The sizes of the INFs are seen to have a negligible effect on the main emission wavelength. For instance, the emission peaks are located at around 435 nm upon excitation at 370 nm for the three INFs.

To inspect the passivation effect provided by the IL bearing a $-SO_3H$ group and other hydrophilic groups on the surface of CDs, the emission spectra of the INFs' dilute aqueous solutions were also measured at room temperature. It can be inferred from Figure 5b,d,f that similarly to the situation found in the case of the bulk INFs, all the emission spectra from the aqueous solutions show excitation-dependent behavior characterized by a red-shift of the emission wavelength and a decrease in the emission intensity.

The excitation spectra for the INFs and corresponding aqueous solutions are given in Figure S6 (left column and right column, respectively). For the INFs, the excitation wavelengths are at 290, 300−400, and 430 nm, corresponding to the main spectral regions in the UV−visible absorption spectra, indicating that the excitation is from the CD absorption in the INFs. The fact that the main excitation bands for the IL_1Il_2 mixture are located below 400 nm (Figure S5e) further reinforces the fact that the emissions of the INFs originate from CDs.

The values of the absolute quantum yield (Φ) for the INFs and corresponding aqueous solutions are listed in Table 1. The

Table 1. Absolute Emission Quantum Yield (Φ) Values as a Function of the Excitation Wavelength (λ_{exc}) for the INFs

sample	λ_{exc} (nm)	Φ	
		INF	aqueous solution
$SFIL_1L_2$-3h	410	0.05 ± 0.01	0.01
	500	0.06 ± 0.01	<0.01
	600	0.01 ± 0.01	<0.01
$SFIL_1L_2$-4h	410	0.09 ± 0.01	0.01
	500	0.08 ± 0.01	<0.01
	600	0.06 ± 0.01	<0.01
$SFIL_1L_2$-5h	250	<0.01	0.003
	410	0.08 ± 0.01	<0.01
	500	0.08 ± 0.01	<0.01

functional groups belonging to IL_1 and IL_2 are believed to be bonded to the surface of the CDs by either coordination or electrostatic interactions and can modify the surface defects, leading to more effective radiative recombination of surface-confined electrons and holes, thus increasing the Φ values.[79] Upon increasing the reaction time from 3 to 4 h, the values of Φ increased from 0.05 ± 0.01 to 0.09 ± 0.01, excited at 410 nm. The latter value is comparable to that reported for the MW-assisted synthesis of SF-based CDs[73] but higher than that obtained for cellulose-derived CDs using acidic IL as a catalyst.[21] When the reaction time was further extended to 5 h, the Φ value decreased slightly, changing from 0.09 ± 0.01 to 0.08 ± 0.01 excited at 410 nm, probably due to the loss of functional groups which accompanied the decrease in the CD size (2.10 ± 0.80 nm), thereby demonstrating the passivation role exerted by the ILs on the luminescence properties. The very low Φ values (around 0.01) measured for the aqueous solution samples are tentatively correlated with the loss of most functional groups as there are many defects on the surface of the bare CDs.

Thermal Features of the INFs. The heat capacities of the IL_1IL_2 mixture and $SFIL_1IL_2$-3h as a function of temperature, shown in Figure 6a, allow inferring that the heat capacity (C_p) increases with temperature. Out of the set of the three INFs, the $SFIL_1IL_2$-3h was chosen for the C_p measurements on account of its best performance under solar-simulated radiation (Figure 6b). Similar values for both IL_1IL_2 mixture and $SFIL_1IL_2$-3h INF were obtained in the initial 285−298 K (12−25 °C) range. Above this interval, a subtle decrease in C_p is observed, which is more pronounced for the IL_1IL_2 mixture, with a minimum at 308 K (35 °C). At higher temperatures, C_p rises continuously until the maximum temperature analyzed is reached. The observed behavior of C_p has been related mainly to the modification of the interactions between nanoparticle surfaces and IL ions with temperature, since their complex nature (hydrogen bonding, van der Waals interactions, electrostatic forces, etc.) can lead to rearrangements in the organization of IL ions in the vicinity of the nanoparticle surfaces. For example, layering of IL molecules around such surfaces due to adsorption as a semisolid layer with better

https://doi.org/10.1021/acs.chemmater.3c01370
Chem. Mater. 2024, 36, 1136−1152

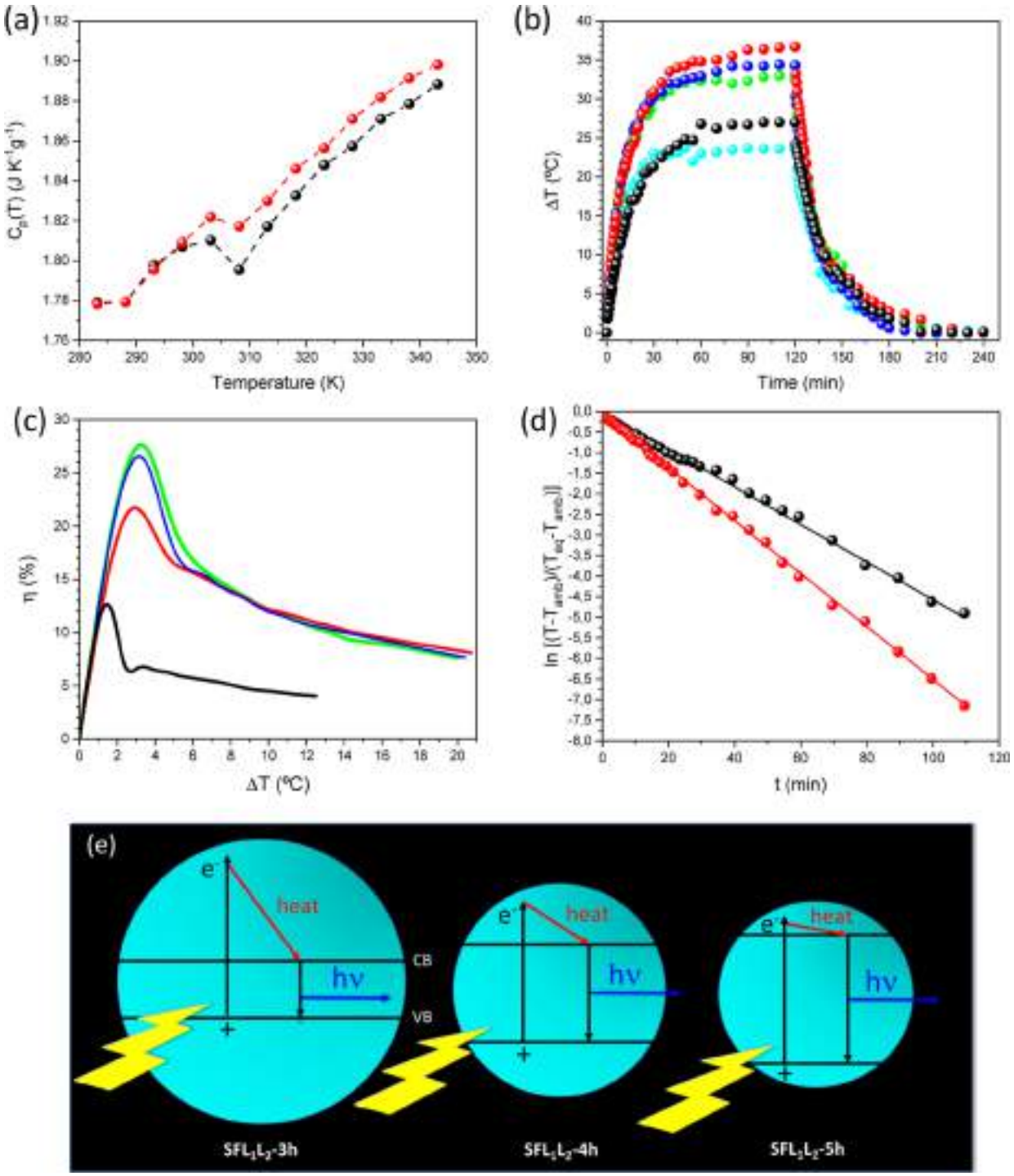

Figure 6. (a) Variation of C_p with temperature within the 12−72 °C interval. (b) Heating−cooling curves upon irradiation at a fluency of 1 Sun. (c) Variation of photothermal conversion efficiency (η_{pc}) with temperature. (d) Plot of $\ln\left(\frac{T(t)-T_{amb}}{T_{eq}-T_{amb}}\right)$ vs t for the cooling stage of the light-induced heating−cooling cycles. Pure water (cyanide symbols), IL_1IL_2 mixture (black line/symbols), $SFIL_1IL_2$-3h (red line/symbols); $SFIL_1IL_2$-4h (blue line/symbols) and $SFIL_1IL_2$-5h (green line/symbols). (e) Schematic representation of the mechanism of absorption/emission of light and heat generation of the INFs. CB and VB stand for conduction band and valence band, respectively.

thermal properties and/or the development of strong overlapping interactions between adjacent mesolayers have been reported.[80] In particular, previous works have shown that the IL semisolid-like liquid ordering onto the surface of the nanoparticles would be the most common mechanism, as also observed for CNTs,[81,82] boron nitride,[83] graphene,[84] and alumina nanoparticles,[85] among others. The anomalous event discerned around 308 K (35 °C) can be attributed to the reversible thermotropic transition undergone by [Bmim][Cl],[86] related to a change in the conformation of the butyl chain from *trans*−*trans* to *trans*−*gauche*.[87]

https://doi.org/10.1021/acs.chemmater.3c01370
Chem. Mater. 2024, 36, 1136−1152

The thermal conductivities of the IL_1IL_2 mixture and $SFIL_1IL_2$-3h at 25 °C were found to be 0.18 ± 0.02 and 0.23 ± 0.03 W m^{-1} K^{-1}, respectively. Both values are larger than those obtained for other INFs composed of, for example, CNTs/1-octyl-3-methylimidazolium hexafluorophosphate ([Omim][PF_6]) + 1-octadecyl-3-methylimidazolium hexafluorophosphate ([Odmim][PF_6]) and CNTs/[Omim][PF_6] + 1-octadecyl-3-methylimidazolium tetrafluoroborate ([Odmim][BF_4]),[27] CNTs/[P66614][$N(CN)_2$], CNTs/1-ethyl-3-methylimidazolium thiocyanate ([Emim][SCN]), CNTs/[Bmim][SCN],[88] Al_2O_3/[Emim]Cl,[89] MgO/[Emim]-[$N(CN)_2$] and MgO/1-ethyl-3-methylimidazolium tricyanomethanide ([Emim][TCM]),[90] or fullerene/[Emim][SCN], graphite/[Emim][SCN], graphene/[Emim][SCN], CNTs/[Emim][SCN], and carbon black/[Emim][SCN].[91] To explain this evidence, it is important to recall that in general, suspended nanoparticles substantially enhance the effective thermal conductivity because the ratio of surface to volume is high in comparison with suspension of micron-size solid particles. This would be the case in our CDs, with very small sizes of a few nanometers compared to CNTs, graphene, or other nanoparticles, which exhibit much larger dimensions. Hence, this would allow an enhancement of the interfacial layer of ordered atoms of the base fluid near the boundary of the solid nanoparticle, which can be considered as a thermal bridge between base liquid and solid nanoparticle, concomitantly increasing the thermal conductivity of INFs. We cannot discard either Brownian motion, which would be more important for our smaller CDs, additionally increasing energy transfer, an effect becoming more marked with the temperature increase. Nevertheless, the exact knowledge of the involved intermolecular interactions and organization of layers, among other factors, should be precisely known in order to acquire a full understanding of the achieved thermal conductivity values.

The heating and cooling profiles of the three synthesized INFs ($SFIL_1IL_2$-3h, $SFIL_1IL_2$-4h, and $SFIL_1IL_2$-5h), and the base nanofluid, i.e., the IL_1IL_2 mixture, and pure water as controls were examined under illumination at an irradiation of 1 Sun (i.e., 1120 W m^{-2}). Figure S7 shows the heating−cooling setup employed for $SFIL_1IL_2$-3h. Figure 6b demonstrates that the temperature rapidly increased under the solar-simulated radiation and then progressively reached a steady state due to the increasing importance of heat dissipation as the temperature differences between the INF and the surrounding environment increased.[92] Finally, the temperature dropped quickly to room temperature after the light irradiation source was turned off. The observed behavior can be explained as follows. When the INF is exposed to a light irradiation source, it absorbs the incident light and converts it into heat at a constant rate. Then, the INF temperature quickly rises as the heat dissipation rate is very low due to the initial negligible temperature difference between the INF and the surrounding environment. As such a temperature difference increases during heating, heat dissipation becomes more significant (the so-called heating stage).[47] When the INF temperature reaches its equilibrium value (T_{eq}), the heat generation rate equals the heat dissipation rate. After turning off the excitation, heat dissipation becomes predominant, causing the INF to cool down back to ambient temperature. From the light heating experiments, we conclude that the different INFs reach the thermal equilibrium at ca. 120 min, with maximal temperature increases of ca. 36.7, 34.4, and 33.0 °C for $SFIL_1IL_2$-3h, $SFIL_1IL_2$-4h, and $SFIL_1IL_2$-5h, respectively, compared to ca. 27.0 and 23.7 °C for the IL_1IL_2 mixture and pure water, respectively (Figure 6b). These facts confirm the successful light absorbance and subsequent conversion of light into heat provided by the SF-based INFs.

It is of interest to discuss at this stage the reason for the larger temperature increment (ΔT) found for the IL_1IL_2 mixture with respect to water under the irradiation test performed (Figure 6b). Figure 6a demonstrates that the C_p values of the IL_1IL_2 mixture are within ca. 1.78−1.88 J K^{-1} g^{-1} in the 283−345 K temperature interval here measured, whereas the C_p of water is barely constant at 4.21−4.18 J K^{-1} g^{-1} over the same temperature range. Considering that the C_p is defined as the energy required to raise the temperature 1 K in 1 g of material, we may then expect that a similar illumination energy input which is transformed into heat after relaxation would involve a larger ΔT for the IL_1IL_2 mixture than for pure water. Also, it must be noted that the IL_1IL_2 mixture shows a weak absorption maximum, peaking at ca. 310 nm, and a strong absorption increase at shorter wavelengths (far-UV) from ca. 245 nm (Figure S5e), as is also observed for water which, it is worth remembering, has a rather low absorption cross section. Moreover, there exist emission bands at around 340 nm in the IL_1IL_2 mixture (Figure S5f) which can be attributed to the emission from IL_1, and the excitation-dependent emission bands can be due to the emission of IL_1 and IL_2. This is, therefore, indicative of the more complex optical behavior of the IL_1IL_2 mixture compared to water and even to the independent IL_1 and IL_2. The latter also have different optical properties, as observed, for example, in Figure S5a−d, respectively. Thus, the ability of the IL_1IL_2 mixture to gain light energy, promoting its relaxation through both radiative and nonradiative mechanisms, is clearly a consequence of its much more complex molecular composition and organization compared to that of water molecules. The same conclusions may be drawn from the comparison of the transmittance spectrum of water with those of two series of aqueous solutions with increasing concentrations of IL_1IL_2 mixture (Figure S8a) and $SFIL_1IL_2$-3h (Figure S8b). The transmittance spectrum of water exhibits a plateau above 90% between 400 and 950 nm and two characteristic absorption peaks at 977 and 1200 nm (Figure S8a,b, black line). The spectrum of the most dilute solution tested (IL_1IL_2/0.33%) essentially coincides with the spectrum of water (Figure S8a, cyanide line). When the concentration of the solution is increased 2-fold (IL_1IL_2/0.66%), the spectrum suffers a significant reduction (Figure S8a, green line). Minor transmittance changes occur for IL_1IL_2/1.00% and IL_1IL_2/1.33% (Figure S8a, violet and red lines, respectively). The most marked effect occurred, however, for the highest concentration considered, i.e., IL_1IL_2/1.66% (Figure S8a, blue line). The behavior exhibited by the aqueous solutions of $SFIL_1IL_2$-3h with the same range of concentrations reveals that the influence of $SFIL_1IL_2$-3h is considerably more important than that of IL_1IL_2 (Figure S8b). The drop observed in the transmittance values in both series of solutions may be interpreted as an indication that as the concentration of IL_1IL_2 and $SFIL_1IL_2$-3h increases in the solution, the interplay between the CDs is enhanced, favoring scattering and thus leading to an increase in absorption. However, this effect is definitely more drastic in the case of the $SFIL_1IL_2$-3h-based solutions. In the spectrum of $SFIL_1IL_2$-3h/1.66%, the characteristic absorption bands of water are weaker and ill-

https://doi.org/10.1021/acs.chemmater.3c01370
Chem. Mater. 2024, 36, 1136−1152

defined. Moreover, the water plateau corresponds to a transmittance reduction of about 60% (Figure S8b, blue line).

From the heating experimental data, the solar-thermal conversion efficiency η was first calculated according to eq 1, that is, not considering thermal dissipation. Figure 6c shows the temperature dependence of η_{pc} for the IL_1IL_2 mixture (as control) and the three INFs. Considering solely the heating process, the expected temperature-dependent behavior is observed for η_{pc}. Among these, $SFIL_1IL_2$-5h showed a slightly larger photothermal conversion efficiency (ca. 27.2%) compared to $SFIL_1IL_2$-4h (26.0%) and $SFIL_1IL_2$-3h (21.7%), whereas the IL_1IL_2 mixture reached a value of only ca. 11.6%. The obtained profiles and values of the photothermal conversion efficiencies are similar to those obtained for other INFs composed of, for example, CDs or graphene oxide.[18,93]

The rate constant of heat dissipation (B) for the different samples was also calculated using eq 2. Its linear plot is shown in Figure 6d for the IL_1IL_2 mixture and the $SFIL_1IL_2$-3h INF as examples. Table 2 demonstrates that the slightly largest rate constant corresponds to $SFIL_1IL_2$-3h, followed by $SFIL_1IL_2$-4h and $SFIL_1IL_2$-5h; however, all values are larger than that of the pure IL_1IL_2 mixture. The photothermal conversion energy is η_{pc}, considering that thermal dissipation was determined using eq 6. The as-derived values are depicted in Table 2. $SFIL_1IL_2$-3h shows the best efficiency among the three INFs (9.8%).

Table 2. Photothermal Conversion Efficiency, η_{pc}, Rate Constant of Heat Dissipation, B, Equilibrium, T_{eq}, Initial Ambient, T_{amb}, Temperatures, and Sample Mass Used in Light Irradiation Experiments

sample	T_{amb} (°C)	T_{eq} (°C)	m (g)	10^{-4} B (s^{-1})	η_{pc}
IL_1IL_2 mixture	23.4	50.5	2.46	7.6	4.0
$SFIL_1IL_2$-3h	24.2	61.2	2.95	11.5	9.8
$SFIL_1IL_2$-4h	25.7	60.4	2.83	11.1	8.9
$SFIL_1IL_2$-5h	22.7	55.8	2.88	10.4	8.0

It is of interest to comment on the differences observed in the heating−cooling curves and in the corresponding photothermal conversion efficiencies. These may arise from the potential slight differences in the optical properties and, thus, in the band gap energies of the fabricated INFs. As inferred from the TEM images represented in Figure 1, the size of the synthesized CDs showed slight differences, decreasing from 3.82, to 2.47 and then to 2.10 for $SFIL_1IL_2$-3h, $SFIL_1IL_2$-4h, and $SFIL_1IL_2$-5h, respectively. Typically, such size changes are a consequence of the loss of functional groups. Since the size of CDs in derived INFs follows the sequence $SFIL_1IL_2$-3h > $SFIL_1IL_2$-4h > $SFIL_1IL_2$-5h, the observed temperature increments and photothermal conversion efficiencies would correlate with the increase in the CDs' band gap upon decreasing the particle size[94] and the subsequent difference between the incident photon energy and the electronic gap being wasted as heat which might elevate the temperature of the surroundings (Figure 6e). Therefore, the reduction of the band gap can enhance the photoconversion efficiency. Indeed, the latter is larger in the case of $SFIL_1IL_2$-3h and thus, in perfect agreement with the obtained efficiency data when calculated with the equation including the thermal losses. In addition, the different synthesis times may have led to slightly different decomposition states of the SF protein, which in any case is not complete, and, thus, we have the resulting organization of the SF residual chains and ILs molecules surrounding the CDs. Moreover, XPS data also reflect slight changes in binding energies for heteroatom signals, particularly for N and O, which are also known to affect band gap energy. In summary, any chemical/physical modification that affects the band gap energy in CDs can give rise to changes in their capacity for light absorption and, subsequently, in the photoconversion efficiency of the INFs.

Finally, the temperature distribution profile upon irradiation of the $SFIL_1IL_2$-3h INF at different times was monitored with a thermal camera. Figure 7 shows that there exists a temperature gradient in the sample, with a hotter region corresponding to the area directly irradiated by the light and behind it; the heat is then distributed along the remainder of the sample. It is observed that as the irradiation time increases, the temperature becomes higher, not only in the illuminated area but also in the surroundings, as a consequence of the thermal diffusion (Figure 7b,c). In addition, it also corroborates the presence of

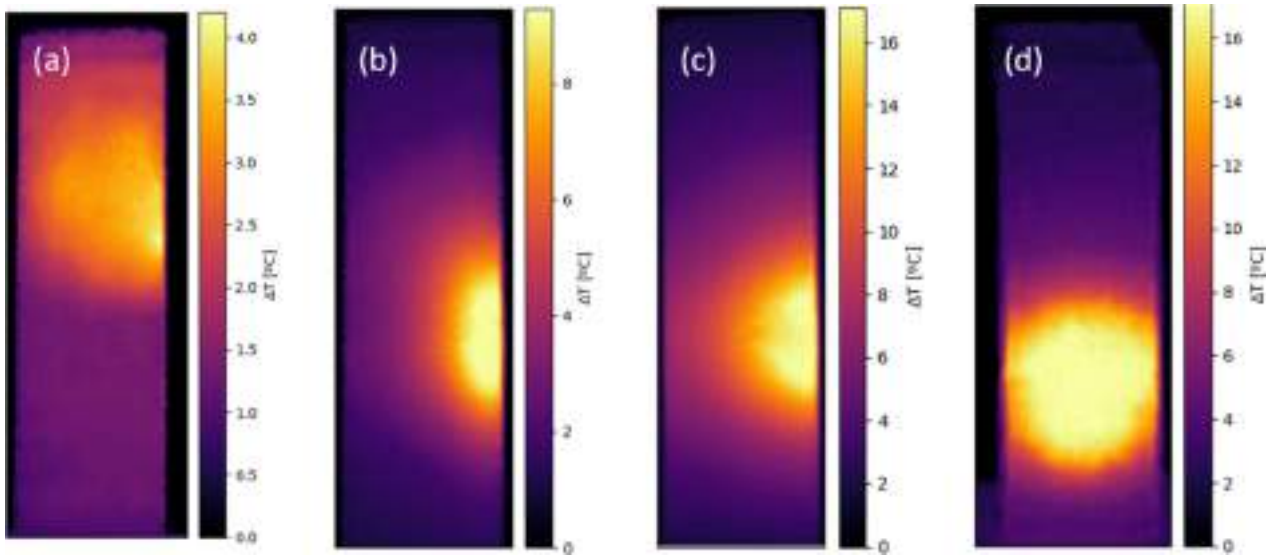

Figure 7. Temperature distribution under light illumination detected with a thermal camera. (a) IL_1IL_2 mixture after 10 min of irradiation. $SFIL_1IL_2$-3h after 5 (b) and 10 min of irradiation with (c) side and (d) front views of the irradiated sample cell.

https://doi.org/10.1021/acs.chemmater.3c01370
Chem. Mater. 2024, 36, 1136−1152

the CDs in the base IL mixture favoring the achievement of larger temperatures when compared to the neat IL_1IL_2 liquid mixture (Figure 7a).

To get insight into the stability of the INFs, a reusability test was performed with $SFIL_1IL_2$-5h. Figure 8 shows that the

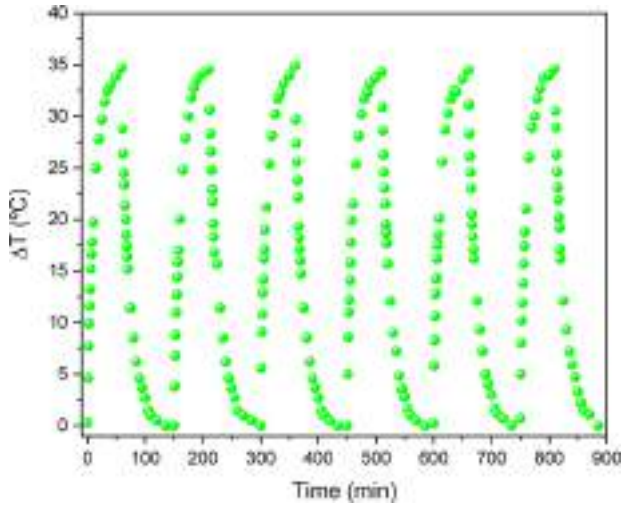

Figure 8. Reusability test of $SFIL_1IL_2$-5h (irradiation duration of 60 min at 1 Sun illumination intensity and cooldown period of 90 min).

variation of temperature ΔT between the different cycles remained essentially constant (34.7, 34.5, 34.9, 34.3, 34.5, and 34.6 °C from the first to the sixth cycles, respectively). The TEM image reproduced in Figure S9a demonstrates that the particle size of the CDs in the sample was preserved after the reutilization. After the sixth heating−cooling cycle, the dimension of the CDs was 2.15 ± 0.46 nm versus 2.10 ± 0.80 nm prior to cycling. Therefore, we are led to deduce that the band gap of the CDs remained the same during several cycles, thus being in accordance with the similar temperature variation between cycles (Figure 8). The TGA curves of $SFIL_1IL_2$-5h recorded before and after cycling, represented in Figure S9b, indicate that the cycled sample contained slightly more water (Figure S9b, red line) than the noncycled sample (Figure S9b, black line) (water loss of 13 and 9%, respectively). The UV−visible absorption spectrum of cycled $SFIL_1IL_2$-5h shows a new band at 450 nm (Figure S9c, red line), and both the excitation and emission spectra reveal a red shift after the reutilization test, pointing out that the absorption of water affected the optical properties of the CDs. Comparison of the temperature dependence of the C_p of reutilized (Figure S9f, red line) and as-synthesized (Figure S9f, black line) $SFIL_1IL_2$-5h allows concluding that cycling induced an increment of C_p of about 0.20 J K^{-1} g^{-1} within the whole interval of temperatures considered. This effect may be associated with the presence of additional water in the cycled sample. In conclusion, we may state that $SFIL_1IL_2$-5h has remarkable stability over a long period of time and over the whole range of the working temperatures.

■ CONCLUSIONS

There is a pressing need for new processes and new material systems able to tackle the main challenges imposed by advanced thermal technologies in terms of sustainability and heat transfer enhancement. In this context, we propose attractive INFs incorporating CDs produced from *B. mori*-based SF dispersed in a mixture of [Bmim][Cl] and [SBmim][Trif] ILs. While the former IL acts primarily as a SF solvent, the latter IL promotes the disruption of the SF chains. Their functional groups remain at the surface of the CDs. The synthesis is simple and relatively fast and does not require any purification steps. Reaction times of 3, 4, and 5 h were tested, yielding uniform spherical CDs with average diameters of 3.82 ± 0.86, 2.47 ± 0.60, and 2.10 ± 0.80 nm, respectively, and revealing the presence of graphene diffraction planes.

The novel INFs are essentially viscous fluids with shear thinning behavior at high shear rates. Remarkably, the presence of SF-based CDs considerably enhances the viscoelastic properties when compared with the neat mixture of ILs. The $SFIL_1IL_2$-4h shows the highest shear viscosity and viscoelasticity (both G' and G''). Interestingly, this was the most efficient system in terms of photothermal conversion. Due to the inherent complexity of these systems, interparticle and IL ion interactions and reorganization are expected to strongly affect not only the rheological performance but also the thermal features.

The INF samples display efficient emission with a quantum yield up to 0.09 in the visible spectral range under UV/blue irradiation. The emission peak position red-shifts as the excitation wavelength increases, suggesting a luminescence mechanism involving surface state energy levels from the various functional groups present on the surface of the CDs.

Under conditions mimicking solar irradiation, the obtained INFs are able to transform light into heat, with maximum photothermal conversion efficiencies above 20%. The synthesized SF-derived CDs and the subsequent rearrangement of IL molecules around their surfaces play here a key role in enhancing both the INF heat capacity and thermal conductivity compared to the situation in the base fluid.

The reusability test carried out confirmed the high stability of the INFs over time in the working temperature interval.

We foresee that the present family of INFs, which relies on an extremely versatile, yet simple, design concept, will soon yield a wide range of other attractive systems. Changes in the reaction conditions and in the nature and relative proportion of the ILs are expected to give rise to a wide variety of materials with fine-tailored properties. For instance, recent results of ongoing work allow us to state, as we write, that the increase in reaction time plays a key role in the optical features of the INFs. Anyway, for the sake of clarity, it is essential to stress that the reaction conditions employed in the present work were not established at random. They are the result of a thorough, systematic, and time-consuming optimization that enabled us to establish the threshold parameters, i.e., the conditions that guarantee the formation of the $SFIL_1IL_2$ INFs: (1) the IL_1/SF stoichiometry (10/1 weight ratio), which was dictated by the minimum amount of IL_1 ([Bmim][Cl]) required to dissolve the SF powder at 100 °C; (2) the IL_2/SF stoichiometry, which was based on previous reports for the synthesis of INFs with polysaccharides but especially on the practical observation that the decrease in the amount of IL_2 did not promote the synthesis reaction; (3) the selection of IL_2 ([SBmim][Trif]), chosen out of a set of other ILs also bearing sulfate groups which were also tested, but with no success; (4) the temperature for the dissolution step (100 °C), which corresponds to the minimum temperature for IL_1 to dissolve the β-sheets of SF; and (5) the synthesis temperature (80 °C), which represents the minimum temperature required to initiate

https://doi.org/10.1021/acs.chemmater.3c01370
Chem. Mater. 2024, 36, 1136−1152

the reaction. In the future, important aspects, such as the influence of humidity or contaminants, among others, will have to be investigated.

Overall, the results reported open the door to a new series of exciting INFs offering excellent prospects, not only for the domain of heat transfer fluids but also for other related fields. Unpublished work demonstrates that these INFs are excellent candidates as active layers of smart thermotropic windows and electrochromic windows.

■ ASSOCIATED CONTENT

Supporting Information

The Supporting Information is available free of charge at https://pubs.acs.org/doi/10.1021/acs.chemmater.3c01370.

Chemical formulas of SF repeat unit, IL_1 and IL_2, and color emitted by the INFs under irradiation with a UV lamp at 365 nm, ATR/FTIR spectra of the INFs and IL_1IL_2 mixture, XPS spectra of the $SFIL_1IL_2$-4h and $SFIL_1IL_2$-5h INFs and of the IL_1IL_2 mixture, TGA curves of the INFs and IL_1IL_2 mixture, room-temperature UV−visible absorption spectrum of the IL_1IL_2 aqueous solution, excitation and emission spectra of IL_1, IL_2, and IL_1IL_2, excitation spectra of the INFs in bulk and in aqueous solution, visible and thermal images of $SFIL_1IL_2$-3h taken during the heating−cooling measurements under irradiation with a solar simulator, transmittance spectra of water and aqueous solutions of IL_1IL_2 and SFL_1L_2-3h, TEM image, TGA curves, and room-temperature UV−visible absorption spectra of an aqueous solution of $SFIL_1IL_2$-5h before and after the recyclability test, excitation and emission spectra of $SFIL_1IL_2$-5h after reutilization, variation of Cp with temperature within the 12-72 °C interval of $SFIL_1IL_2$-5h before and after the recyclability test (PDF)

■ AUTHOR INFORMATION

Corresponding Authors

Tiago A. G. Duarte − *CQ-VR, University of Trás-os-Montes e Alto Douro, 5001-801 Vila Real, Portugal*; Email: tduarte@utad.pt

Verónica de Zea Bermudez − *CQ-VR, University of Trás-os-Montes e Alto Douro, 5001-801 Vila Real, Portugal; Chemistry Department, University of Trás-os-Montes e Alto Douro, 5001-801 Vila Real, Portugal;* orcid.org/0000-0002-7577-4938; Email: vbermude@utad.pt

Authors

Rui F. P. Pereira − *Chemistry Center and Chemistry Department, University of Minho, 4710-057 Braga, Portugal;* orcid.org/0000-0001-7279-5728

Bruno Medronho − *MED—Mediterranean Institute for Agriculture, Environment and Development, CHANGE−Global Change and Sustainability Institute, Faculdade de Ciências e Tecnologia, Universidade do Algarve, 8005-139 Faro, Portugal; Surface and Colloid Engineering, FSCN Research Centre, Mid Sweden University, SE-851 70 Sundsvall, Sweden;* orcid.org/0000-0003-0972-1739

Elizaveta S. Maltseva − *EnergyLab, ChemBio Cluster, ITMO University, 191002 Saint Petersburg, Russia*

Elena F. Krivoshapkina − *EnergyLab, ChemBio Cluster, ITMO University, 191002 Saint Petersburg, Russia;* orcid.org/0000-0001-6981-5134

Alejandro Varela-Dopico − *Colloids and Polymer Physics Group (GFCP), Condensed Matter Physics Area, Faculty of Physics, Universidade de Santiago de Compostela, 15782 Santiago de Compostela, Spain*

Pablo Taboada − *Colloids and Polymer Physics Group (GFCP), Condensed Matter Physics Area, Faculty of Physics, Universidade de Santiago de Compostela, 15782 Santiago de Compostela, Spain;* orcid.org/0000-0002-2903-7857

Lianshe Fu − *Department of Physics, CICECO−Aveiro Institute of Materials, University of Aveiro, 3810-193 Aveiro, Portugal*

Rute A. S. Ferreira − *Department of Physics, CICECO−Aveiro Institute of Materials, University of Aveiro, 3810-193 Aveiro, Portugal;* orcid.org/0000-0003-1085-7836

Complete contact information is available at: https://pubs.acs.org/10.1021/acs.chemmater.3c01370

Author Contributions

The syntheses were performed by T.A.G.D. and E.S.M. Experimental data were collected by T.A.G.D., R.F.P.P., B.M., E.S.M., A.V.D., P.T., and L.F. The manuscript was co-written by T.A.G.D., R.F.P.P., B.M., E. F. K., P.T., L.F., R.A.S.F., and V.D.Z.B. The work was proposed by V.D.Z.B.

Funding

This work was funded by OBTAIN-Objective Sustainability (NORTE-01-0145-FEDER-000084), cofinanced by the European Regional Development Fund (FEDER) through NORTE 2020 (Northern Regional Operational Programme 2014/2020), SOLPOWINS-Solar-Powered Smart Windows for Sustainable Buildings (PTDC/CTM/4304/2020), CENTRO2020 in the scope of the project PLANETa (CENTRO-01-0247-FEDER-181242), UIDB/00616/2020 and UIDP/00616/2020, CICECO-Aveiro Institute of Materials, and UIDB/50011/2020, UIDP/50011/2020, and LA/P/0006/2020, financed by national funds through the FCT/MCTES (PIDDAC).

Notes

The authors declare no competing financial interest.

■ ACKNOWLEDGMENTS

R.F.P.P. acknowledges FCTUMinho for his contract in the scope of Decreto-Lei 57/2016 57/2017. E.S.M. is grateful for the Erasmus+ grant that funded her stay at CQ-VR. E.F.K. thanks state task no. FSER-2022-0002 within the framework of the National Project "Science and Universities". P.T. thanks Agencia Estatal de Investigación (AEI) by project PID2019-109517RB-I00 and Xunta de Galicia by grant ED431C 2022/18. ERDF funds are also acknowledged. Vicente Domínguez, Francisco Rivadulla, and Carmen Alvarez-Lorenzo, from USC, are acknowledged for their helpful assistance during heat capacity, thermal conductivity, and thermal imaging acquisition measurements, respectively. Sandra Correia, from IT, is acknowledged for recording the emission spectra.

■ REFERENCES

(1) Agency, I. E. *World Energy Outlook 2022*, 2022.

(2) Govindasamy, D.; Kumar, A. Experimental analysis of solar panel efficiency improvement with composite phase change materials. *Renewable Energy* **2023**, *212*, 175−184.

(3) Batagiannis, P. K. Thermal assessment of silicon-based composite materials used in photovoltaics. In *International Solar nergy Society UK Section - Conferenc C*, 2001; pp 151−157.
(4) Krauter, S.; Hanitsch, R.; Wenham, S. R. Simulation of thermal and optical performance of PV modules, Part III. *Renewable Energy* **1994**, *5*, 1701−1703.
(5) Krauter, S.; Hanitsch, R.; Wenham, S. R. Simulation tool for prediction and optimization of output power considering thermal and optical parameters of PV module encapsulation. In *12th European Photovoltaic Solar Energy Conference*, Amsterdam, Holland, 1994; pp 1194−1197.
(6) Lee, S.; Choi, S. U.-S.; Li, S.; Eastman, J. A. Measuring Thermal Conductivity of Fluids Containing Oxide Nanoparticles. *J. Heat Transfer* **1999**, *121*, 280−289.
(7) Svobodova-Sedlackova, A.; Calderón, A.; Barreneche, C.; Gamallo, P.; Fernández, A. I. Understanding the abnormal thermal behavior of nanofluids through infrared thermography and thermophysical characterization. *Sci. Rep.* **2021**, *11* (1), 4879.
(8) Okonkwo, E. C.; Wole-Osho, I.; Almanassra, I. W.; Abdullatif, Y. M.; Al-Ansari, T. An updated review of nanofluids in various heat transfer devices. *J. Therm. Anal. Calorim.* **2021**, *145*, 2817−2872.
(9) Cuce, E.; Cuce, P. M.; Guclu, T.; Besir, A. B. On the Use of Nanofluids in Solar Energy Applications. *J. Therm. Sci.* **2020**, *29* (3), 513−534.
(10) Menni, Y.; Chamkha, A.; Lorenzini, G.; Kaid, N.; Ameur, H.; Bensafi, M. Advances of nanofluids in solar collectors—a review of numerical studies. *Math. Model. Eng. Probl.* **2019**, *6* (3), 415−427.
(11) Wahab, A.; Hassan, A.; Qasim, M. A.; Ali, H. M.; Babar, H.; Sajid, M. U. Solar energy systems—potential of nanofluids. *J. Mol. Liq.* **2019**, *289*, 111049.
(12) Jha, P.; Das, B.; Gupta, R.; Mondol, J.; Ehyaei, M. Review of recent research on photovoltaic thermal solar collectors. *Sol. Energy* **2023**, *257*, 164−195.
(13) Ibrahim, H.; Sazali, N.; Shah, A. S. M.; Karim, M. S. A.; Aziz, F.; Salleh, W. N. W. A review on factors affecting heat transfer efficiency of nanofluids for application in plate heat exchangerA review on factors affecting heat transfer efficiency of nanofluids for application in plate heat exchanger. *J. Adv. Res. Fluid Mech. Therm. Sci.* **2019**, *60* (1), 144−154.
(14) Sajid, M. U.; Ali, H. M. Recent advances in application of nanofluids in heat transfer devices: a critical review. *Renewable Sustainable Energy Rev.* **2019**, *103*, 556−592.
(15) Nazari, M. A.; Ahmadi, M. H.; Sadeghzadeh, M.; Shafii, M. B.; Goodarzi, M. A review on application of nanofluid in various types of heat pipes. *J. Cent South Univ.* **2019**, *26*, 1021−1041.
(16) Vele, N. S.; Patil, R. K. Review on heat transfer enhancement in car radiator using Nano fluids. In *Proceedings of the International Conference on Industrial Engineering and Operations Management*, Bangkok, Thailand, 2019; pp 527−537.
(17) Obaid, H. N.; Habeeb, M. A.; Rashid, F. L.; Hashim, A. Thermal Energy Storage by Nanofluids. *J. Energy Technol. Pol.* **2013**, *3*, 34−36.
(18) Seifikar, F.; Azizian, S. Super-stable carbon quantum dots nanofluid for efficient solar-thermal conversion. *Energy Convers. Manage.* **2021**, *228*, 113675.
(19) Murali Krishna, V.; Sandeep Kumar, M. Numerical analysis of forced convective heat transfer of nanofluids in microchannel for cooling electronic equipment. *Mater. Today Proc.* **2019**, *17*, 295−302.
(20) Ribeiro, A. P. C.; Lourenço, M. J. V.; Nieto de Castro, C. A. Thermal conductivity of Ionanofluis. In *17th Symposium on Thermophysical Properties*: Boulder, USAA, 2009.
(21) Wang, C.; Wang, C.; Xu, P.; Li, A.; Chen, Y.; Zhuo, K. Synthesis of cellulose-derived carbon dots using acidic ionic liquid as a catalyst and its application for detection of Hg^{2+}. *J. Mater. Sci.* **2016**, *51*, 861−867.
(22) Gonçalves, H. M. R.; Pereira, R. F.; Lepleux, E.; Carlier, T.; Pacheco, L.; Pereira, S.; Valente, A. J.; Fortunato, E.; Duarte, A. J.; de Zea Bermudez, V. Nanofluid based on glucose-derived carbon dots functionalized with [Bmim]Cl for the next generation of smart windows. *Adv. Sustainable Syst.* **2019**, *3* (7), 1900047.
(23) Gonçalves, H. M. R.; Pereira, R. F.; Lepleux, E.; Pacheco, L.; Valente, A. J.; Duarte, A. J.; de Zea Bermudez, V. Non-Newtonian Thermosensitive Nanofluid Based on Carbon Dots Functionalized with Ionic Liquids. *Small* **2020**, *16* (28), 1907661.
(24) Fukushima, T.; Asaka, K.; Kosaka, A.; Aida, T. Fully plastic actuator through layer-by layer casting with ionic-liquid-based bucky gel. *Angew. Chem., Int. Ed.* **2005**, *44*, 2410−2413.
(25) Nieto de Castro, C. A.; Lourenço, M. J. V.; Ribeiro, A. P. C.; Langa, E.; Vieira, S. I. C.; Goodrich, P.; Hardacre, C. Thermal Properties of Ionic Liquids and IoNanofluids of Imidazolium and Pyrrolidinium Liquids. *J. Chem. Eng. Data* **2010**, *55* (2), 653−661.
(26) Dzida, M.; Boncel, S.; Jóźwiak, B.; Greer, H. F.; Dulski, M.; Scheller, Ł.; Golba, A.; Flamholc, R.; Dzido, G.; Dziadosz, J.; Kolanowska, A.; Jędrysiak, R.; Blacha, A.; Cwynar, K.; Zorębski, E.; Bernardes, C. E. S.; Lourenço, M. J. V.; Nieto de Castro, C. A. High-Performance Ionanofluids from Subzipped Carbon Nanotube Networks. *ACS Appl. Mater. Interfaces* **2022**, *14* (45), 50836−50848.
(27) Cavieres, J.; José Inestrosa-Izurieta, M.; Vasco, D. A.; Urzúa, J. I. Ionanofluids based on ionic liquid mixtures, a new approach as an alternative material for solar energy storage. *J. Mol. Liq.* **2022**, *351*, 118677.
(28) Pereira, R. F. P.; Brito-Pereira, R.; Gonçalves, R.; Silva, M. P.; Costa, C. M.; Silva, M. M.; de Zea Bermudez, V.; Lanceros-Méndez, S. Silk Fibroin Separators: A Step Toward Lithium-Ion Batteries with Enhanced Sustainability. *ACS Appl. Mater. Interfaces* **2018**, *10*, 5385−5394.
(29) Pereira, R. F. P.; Gonçalves, R.; Fernandes, M.; Costa, C. M.; Silva, M. M.; de Zea Bermudez, V.; Lanceros-Mendez, S. Bombyx mori Silkworm Cocoon Separators for Lithium-ion Batteries with Superior Safety and Sustainability. *Adv. Sustainable Syst.* **2018**, *2*, 1800098.
(30) Pereira, R. F. P.; Gonçalves, R.; Gonçalves, H.; Correia, D. M.; Costa, C. M.; Silva, M. M.; Lanceros-Méndez, S.; de Zea Bermudez, V. Plasma-treated Bombyx mori cocoon separators for high-performance and sustainable lithium-ion batteries. *Mater. Today Sustain.* **2020**, *9*, 100041.
(31) Fernandes, T. C. D.; Rodrigues, H. M. R.; Paz, F. A. A.; Sousa, J. F. M.; Valente, A. J. M.; Silva, M. M.; de Zea Bermudez, V.; Pereira, R. F. P. Highly Conducting Bombyx mori Silk Fibroin-Based Electrolytes Incorporating Glycerol, Dimethyl Sulfoxide and [Bmim]-PF6. *J. Electrochem. Soc.* **2020**, *167* (7), 070551.
(32) Medronho, B.; Filipe, A.; Napso, S.; Khalfin, R. L.; Pereira, R. F. P.; de Zea Bermudez, V.; Romano, A.; Cohen, Y. Silk fibroin dissolution in tetrabutylammonium hydroxide aqueous solution. *Biomacromolecules* **2019**, *20* (11), 4107−4116.
(33) Meng, W.; Bai, X.; Wang, B.; Liu, Z.; Lu, S.; Yang, B. Biomass-Derived Carbon Dots and Their Applications. *Energy Environ. Mater.* **2019**, *2* (3), 172−192.
(34) Wee, S. S.; Ng, Y. H.; Ng, S. M. Synthesis of fluorescent carbon dots via simple acid hydrolysis of bovine serum albumin and its potential as sensitive sensing probe for lead (II) ions. *Talanta* **2013**, *116*, 71−76.
(35) Liu, X.; Li, T.; Hou, Y.; Wu, Q.; Yi, J.; Zhang, G. Microwave synthesis of carbon dots with multi-response using denatured proteins as carbon source. *RSC Adv.* **2016**, *6* (14), 11711−11718.
(36) Wu, Z. L.; Zhang, P.; Gao, M. X.; Liu, C. F.; Wang, W.; Leng, F.; Huang, C. Z. One-pot hydrothermal synthesis of highly luminescent nitrogen-doped amphoteric carbon dots for bioimaging from Bombyx mori silk - natural proteins. *J. Mater. Chem. B* **2013**, *1* (22), 2868−2873.
(37) Li, S.; Wang, H.; Lu, H.; Liang, X.; Wang, H.; Zhang, M.; Xia, K.; Yin, Z.; Zhang, Y.; Zhang, X.; Zhang, Y. Sustainable Silk-Derived Multimode Carbon Dots. *Small* **2021**, *17* (44), 2103623.
(38) Savanur, H. M.; Kalkhambkar, R. G.; Aridoss, G.; Laali, K. K. $[bmim(SO_3H)]$ [OTf]/[bmim] [X] and $Zn(NTf_2)_2$/[bmim] [X] (X = PF_6 and BF_4); efficient catalytic systems for the synthesis of

https://doi.org/10.1021/acs.chemmater.3c01370
Chem. Mater. 2024, 36, 1136−1152

tetrahydropyrimidin-ones (-thiones) via the Biginelli reaction. *Tetrahedron Lett.* **2016**, *57* (27−28), 3029−3035.
(39) Nandi, G. C.; Laali, K. K. Schmidt reaction in ionic liquids: highly efficient and selective conversion of aromatic and hetero-aromatic aldehydes to nitriles with [BMIM(SO_3H)] [OTf] as catalyst and [BMIM] [PF_6] as solvent. *Tetrahedron Lett.* **2013**, *54* (17), 2177−2179.
(40) Rockwood, D. N.; Preda, R. C.; Yücel, T.; Wang, X.; Lovett, M. L.; Kaplan, D. L. Materials fabrication from Bombyx mori silk fibroin. *Nat. Protoc.* **2011**, *6* (10), 1612−1631.
(41) Cao, M.; Zhao, X.; Gong, X. J. S. Ionic Liquid-Assisted Fast Synthesis of Carbon Dots with Strong Fluorescence and Their Tunable Multicolor Emission. *Small* **2022**, *18* (11), 2106683.
(42) Systat Software GmbH, http://www.systat.de/PDFs/PeakFit_4.12.pdf, acessed Sept 14, 2022.
(43) Lugo, L.; Segovia, J. J.; Martín, M. C.; Fernández, J.; Villamañán, M. A. An experimental setup for isobaric heat capacities for viscous fluids at high pressure: Squalane, bis(2-ethylhexyl) sebacate and bis(2-ethylhexyl) phthalate. *J. Chem. Thermodyn.* **2012**, *49*, 75−80.
(44) Gates, J. A.; Wood, R. H.; Cobos, J. C.; Casanova, C.; Roux, A. H.; Roux-Desgranges, G.; Grolier, J.-P. E. Densities and heat capacities of 1-butanol + n-decane from 298 K to 400 K. *Fluid Phase Equilib.* **1986**, *27*, 137−151.
(45) Coelho de Sousa Marques, M. A.; Guimarey, M. J. G.; Domínguez-Arca, V.; Amigo, A.; Fernández, J. Heat capacity, density, surface tension, and contact angle for polyalphaolefins and ester lubricants. *Thermochim. Acta* **2021**, *703*, 178994.
(46) López-Bueno, C.; Bugallo, D.; Leborán, V.; Rivadulla, F. Sub-μL measurements of the thermal conductivity and heat capacity of liquids. *Phys. Chem. Chem. Phys.* **2018**, *20* (10), 7277−7281.
(47) Meng, Z.; Li, Y.; Chen, N.; Wu, D.; Zhu, H. Broad-band absorption and photo-thermal conversion properties of zirconium carbide aqueous nanofluids. *J. Taiwan Inst. Chem. Eng.* **2017**, *80*, 286−292.
(48) Papaioannou, N.; Titirici, M.-M.; Sapelkin, A. Investigating the Effect of Reaction Time on Carbon Dot Formation, Structure, and Optical Properties. *ACS Omega* **2019**, *4* (26), 21658−21665.
(49) Jaganathan, J. R.; Sivapragasam, M.; Wilfred, C. D. Thermal Characteristics of 1-Butyl-3-Methylimimidazolium Based Oxidant Ionic Liquids. *J. Chem. Eng. Process Technol.* **2016**, 71-6..
(50) Liu, M.; Jia, S.; Gong, Y.; Song, C.; Guo, X. Effective Hydrolysis of Cellulose into Glucose over Sulfonated Sugar-Derived Carbon in an Ionic Liquid. *Ind. Eng. Chem. Res.* **2013**, *52* (24), 8167−8173.
(51) Paschoal, V. H.; Faria, L. F. O.; Ribeiro, M. C. C. Vibrational Spectroscopy of Ionic Liquids. *Chem. Rev.* **2017**, *117* (10), 7053−7112.
(52) Pereira, R. F. P.; Sentanin, F.; Pawlicka, A.; Gonçalves, M. C.; Silva, M. M.; de Zea Bermudez, V. Smart Windows Prepared from Bombyx mori Silk. *ChemElectroChem* **2016**, *3* (7), 1084−1097.
(53) Duah, I. K.; Khaligh, A.; Koç, A.; Başaran, D. D. A.; Tuncel, D. Porphyrin cross-linked conjugated polymer nanoparticles-based photosensitizer for antimicrobial and anticancer photodynamic therapies. *J. Appl. Polym. Sci.* **2022**, *139* (11), 51777.
(54) Villar-Garcia, I. J.; Smith, E. F.; Taylor, A. W.; Qiu, F.; Lovelock, K. R. J.; Jones, R. G.; Licence, P. Charging of ionic liquid surfaces under X-ray irradiation: the measurement of absolute binding energies by XPS. *Phys. Chem. Chem. Phys.* **2011**, *13* (7), 2797−2808.
(55) Niedermaier, I.; Kolbeck, C.; Taccardi, N.; Schulz, P. S.; Li, J.; Drewello, T.; Wasserscheid, P.; Steinrück, H.-P.; Maier, F. Organic Reactions in Ionic Liquids Studied by in Situ XPS. *ChemPhysChem* **2012**, *13* (7), 1725−1735.
(56) Ravi, K.; Biradar, A. V. Highly active and scalable SO_3H functionalized carbon catalyst synthesized from bagasse for transformation of bio-based platform chemicals into fuel precursors and its in-depth characterization studies. *Fuel* **2022**, *321*, 124008.
(57) Hu, Y.; Yang, J.; Tian, J.; Jia, L.; Yu, J.-S. Waste frying oil as a precursor for one-step synthesis of sulfur-doped carbon dots with pH-sensitive photoluminescence. *Carbon* **2014**, *77*, 775−782.
(58) Shao, J.; Liu, J.; Zheng, J.; Carr, C. M. X-ray photoelectron spectroscopic study of silk fibroin surface. *Polym. Int.* **2002**, *51* (12), 1479−1483.
(59) Wang, Q.; Yanzhang, R.; Wu, Y.; Zhu, H.; Zhang, J.; Du, M.; Zhang, M.; Wang, L.; Zhang, X.; Liang, X. Silk-derived graphene-like carbon with high electrocatalytic activity for oxygen reduction reaction. *RSC Adv.* **2016**, *6* (41), 34219−34224.
(60) Radu, I.-C.; Biru, I.-E.; Damian, C.-M.; Ion, A.-C.; Iovu, H.; Tanasa, E.; Zaharia, C.; Galateanu, B. Grafting versus Crosslinking of Silk Fibroin-g-PNIPAM via Tyrosine-NIPAM Bridges. *Molecules* **2019**, *24* (22), 4096.
(61) Singh, S.; Cortes, G.; Kumar, U.; Sakthivel, T. S.; Niemiec, S. M.; Louiselle, A. E.; Azeltine-Bannerman, M.; Zgheib, C.; Liechty, K. W.; Seal, S. Silk fibroin nanofibrous mats for visible sensing of oxidative stress in cutaneous wounds. *Biomater. Sci.* **2020**, *8* (21), 5900−5910.
(62) Hao, Y.; Peng, J.; Hu, S.; Li, J.; Zhai, M. Thermal decomposition of allyl-imidazolium-based ionic liquid studied by TGA-MS analysis and DFT calculations. *Thermochim. Acta* **2010**, *501* (1−2), 78−83.
(63) Motta, A.; Fambri, L.; Migliaresi, C. Regenerated silk fibroin films: Thermal and dynamic mechanical analysis. *Macromol. Chem. Phys.* **2002**, *203* (10−11), 1658−1665.
(64) Jóźwiak, B.; Boncel, S. Rheology of ionanofluids - A review. *J. Mol. Liq.* **2020**, *302*, 112568.
(65) Mishra, P. C.; Mukherjee, S.; Nayak, S. K.; Panda, A. A brief review on viscosity of nanofluids. *Int. Nano Lett.* **2014**, *4* (4), 109−120.
(66) Sharma, A. K.; Tiwari, A. K.; Dixit, A. R. Rheological behaviour of nanofluids: A review. *Renewable Sustainable Energy Rev.* **2016**, *53*, 779−791.
(67) Koca, H. D.; Doganay, S.; Turgut, A.; Tavman, I. H.; Saidur, R.; Mahbubul, I. M. Effect of particle size on the viscosity of nanofluids: A review. *Renewable Sustainable Energy Rev.* **2018**, *82*, 1664−1674.
(68) Nadooshan, A. A.; Eshgarf, H.; Afrand, M. Evaluating the effects of different parameters on rheological behavior of nanofluids: A comprehensive review. *Powder Technol.* **2018**, *338*, 342−353.
(69) Gao, J.; Mwasame, P. M.; Wagner, N. J. Thermal rheology and microstructure of shear thickening suspensions of silica nanoparticles dispersed in the ionic liquid [C_4mim] [BF_4]. *J. Rheol.* **2017**, *61* (3), 525−535.
(70) Wang, B.; Wang, X.; Lou, W.; Hao, J. Rheological and Tribological Properties of Ionic Liquid-Based Nanofluids Containing Functionalized Multi-Walled Carbon Nanotubes. *J. Phys. Chem. C* **2010**, *114* (19), 8749−8754.
(71) Gaylord, N. G.; Van Wazer, J. R. *Viscoelastic Properties of Polymers*; John D. Ferry, Wiley: New York, 1961, p 482.
(72) Xu, Y.; Zheng, Q.; Song, Y. Comparison studies of rheological and thermal behaviors of ionic liquids and nanoparticle ionic liquids. *Phys. Chem. Chem. Phys.* **2015**, *17* (30), 19815−19819.
(73) Ko, N. R.; Nafiujjaman, M.; Cherukula, K.; Lee, S. J.; Hong, S. J.; Lim, H. N.; Park, C. H.; Park, I. K.; Lee, Y. K.; Kwon, I. K. Microwave-Assisted Synthesis of Biocompatible Silk Fibroin-Based Carbon Quantum Dots. *Part. Part. Syst. Charact.* **2018**, *35* (3), 1700300.
(74) Zheng, Y.; Hao, J.; Arkin, K.; Bei, Y.; Ma, X.; Shang, Q.; Che, W. H_2O_2-assisted detection of melamine using fluorescent probe based on corn cob carbon dots-Ionic Liquid-Silver nanoparticles. *Food Chem.* **2023**, *403*, 134415.
(75) Zhu, C.; Zhai, J.; Dong, S. Bifunctional fluorescent carbon nanodots: green synthesis via soy milk and application as metal-free electrocatalysts for oxygen reduction. *Chem. Commun.* **2012**, *48* (75), 9367−9369.
(76) Ding, H.; Yu, S.-B.; Wei, J.-S.; Xiong, H.-M. Full-color light-emitting carbon dots with a surface-state-controlled luminescence mechanism. *ACS Nano* **2016**, *10* (1), 484−491.
(77) Woo, J.; Song, Y.; Ahn, J.; Kim, H. Green one-pot preparation of carbon dots (CD)-embedded cellulose transparent film for Fe^{3+} indicator using ionic liquid. *Cellulose* **2020**, *27*, 4609−4621.

(78) Rizzo, C.; Arcudi, F.; Đorđević, L.; Dintcheva, N. T.; Noto, R.; D'Anna, F.; Prato, M. J. A. n. Nitrogen-doped carbon nanodots-ionogels: preparation, characterization, and radical scavenging activity. *ACS Nano* **2018**, *12* (2), 1296−1305.
(79) Guo, T.; Zheng, A.; Chen, X.; Shu, Y.; Wang, J. The structure-activity relationship of hydrophilic carbon dots regulated by the nature of precursor ionic liquids. *J. Colloid Interface Sci.* **2019**, *554*, 722−730.
(80) Hentschke, R. On the specific heat capacity enhancement in nanofluids. *Nanoscale Res. Lett.* **2016**, *11* (1), 88.
(81) Frolov, A. I.; Kirchner, K.; Kirchner, T.; Fedorov, M. V. Molecular-scale insights into the mechanisms of ionic liquids interactions with carbon nanotubes. *Faraday Discuss.* **2012**, *154* (0), 235−247.
(82) Wang, X.; Fu, F.; Peng, K.; Huang, Q.; Li, W.; Chen, X.; Yang, Z. Understanding of Competitive Hydrogen Bond Behavior of Imidazolium-Based Ionic Liquid Mixture around Single-Walled Carbon Nanotubes. *J. Phys. Chem. C* **2020**, *124* (12), 6634−6645.
(83) Oster, K.; Hardacre, C.; Jacquemin, J.; Ribeiro, A. P. C.; Elsinawi, A. Understanding the heat capacity enhancement in ionic liquid-based nanofluids (ionanofluids). *J. Mol. Liq.* **2018**, *253*, 326−339.
(84) Hermida-Merino, C.; Pereiro, A. B.; Araújo, J. M. M.; Gracia-Fernández, C.; Vallejo, J. P.; Lugo, L.; Piñeiro, M. M. Graphene IoNanofluids, Thermal and Structural Characterization. *Nanomaterials* **2019**, *9*, 1549.
(85) Chereches̨, E. I.; Prado, J. I.; Ibanescu, C.; Danu, M.; Minea, A. A.; Lugo, L. Viscosity and isobaric specific heat capacity of alumina nanoparticle enhanced ionic liquids: An experimental approach. *J. Mol. Liq.* **2020**, *317*, 114020.
(86) Efimova, A.; Hubrig, G.; Schmidt, P. Thermal stability and crystallization behavior of imidazolium halide ionic liquids. *Thermochim. Acta* **2013**, *573*, 162−169.
(87) Ryosuke, O.; Satoshi, H.; Satyen, S.; Akiko, K.; Hiro-o, H. Rotational Isomerism and Structure of the 1-Butyl-3-methylimidazolium Cation in the Ionic Liquid State. *Chem. Lett.* **2003**, *32* (10), 948−949.
(88) França, J. M. P.; Lourenço, M. J. V.; Murshed, S. M. S.; Pádua, A. A. H.; Nieto de Castro, C. A. Thermal Conductivity of Ionic Liquids and IoNanofluids and Their Feasibility as Heat Transfer Fluids. *Ind. Eng. Chem. Res.* **2018**, *57* (18), 6516−6529.
(89) Kanti, P. K.; Chereches, E. I.; Minea, A. A.; Sharma, K. V. Experiments on thermal properties of ionic liquid enhanced with alumina nanoparticles for solar applications. *J. Therm. Anal. Calorim.* **2022**, *147* (23), 13027−13038.
(90) Hothar, M.; Wu, Z.; Sundén, B. Thermal Conductivity of Ionic Liquid-Based Nanofluids Containing Magnesium Oxide and Aluminum Oxide Nanoparticles. *Heat Transfer Eng.* **2022**, *43* (21), 1806−1819.
(91) Jóźwiak, B.; Dzido, G.; Zorębski, E.; Kolanowska, A.; Jędrysiak, R.; Dziadosz, J.; Libera, M.; Boncel, S.; Dzida, M. Remarkable Thermal Conductivity Enhancement in Carbon-Based Ionanofluids: Effect of Nanoparticle Morphology. *ACS Appl. Mater. Interfaces* **2020**, *12* (34), 38113−38123.
(92) Dong, L.; Ding, S.; Wu, Z.; Xie, H.; Wang, J.; Wang, T.; Wang, Y.; Huang, Y. Photothermal Conversion Characteristics of ZnO/MWCNTs Binary Nanofluids and ZnO/MWCNTs/Au Ternary Hybrid Nanofluids in Direct Absorption Solar Collectors. *Energy Technol.* **2022**, *10* (10), 2200661.
(93) Campos, C.; Vasco, D.; Angulo, C.; Burdiles, P. A.; Cardemil, J.; Palza, H. About the relevance of particle shape and graphene oxide on the behavior of direct absorption solar collectors using metal based nanofluids under different radiation intensities. *Energy Convers. Manage.* **2019**, *181*, 247−257.
(94) Barman, M. K.; Patra, A. Current status and prospects on chemical structure driven photoluminescence behaviour of carbon dots. *J. Photochem. Photobiol., C* **2018**, *37*, 1−22.

https://doi.org/10.1021/acs.chemmater.3c01370
Chem. Mater. 2024, 36, 1136−1152